Science
AAAS

# Title: Segregation-induced ordered superstructures at general grain boundaries in a Ni-Bi alloy

**Authors:** Zhiyang Yu[1,†], Patrick R. Cantwell[2], Qin Gao[3], Denise Yin[1], Yuanyao Zhang[4], Naixie Zhou[4], Gregory S. Rohrer[5], Michael Widom[3], Jian Luo[4,*], Martin P. Harmer[1,*]

**Affiliations:**

[1]Department of Materials Science and Engineering, Lehigh University, 5 East Packer Avenue, Bethlehem PA 18015 USA.

[2]Department of Mechanical Engineering, Rose-Hulman Institute of Technology, 5500 Wabash Avenue, Terre Haute IN 47803 USA.

[3]Department of Physics, Carnegie Mellon University, 5000 Forbes Avenue, Pittsburgh PA 15213 USA

[4] Department of NanoEngineering, Program of Materials Science and Engineering, University of California, San Diego, 9500 Gilman Drive, La Jolla, CA 92093 USA.

[5] Department of Materials Science and Engineering, Carnegie Mellon University, 5000 Forbes Avenue, Pittsburgh PA 15213 USA.

*Correspondence to: mph2@lehigh.edu (M.P.H.) and jluo@alum.mit.edu (J.L.)

[†]Current Address: School of Materials Science and Engineering, Xiamen University of Technology, Xiamen 361024, China

**Abstract:** The properties of materials dramatically and sometimes catastrophically change as alloying elements and impurities accumulate preferentially at grain boundaries. Studies of bicrystals show that regular atomic patterns often arise due to this solute segregation at high-symmetry boundaries, but it is not known if superstructures exist at general grain boundaries in polycrystals. We show that ordered, segregation-induced grain boundary superstructures occur at randomly selected general grain boundaries in Bi-doped polycrystalline nickel. We demonstrate that these reconstructions are driven by the orientation of the terminating grain surfaces rather than lattice matching between grains. This discovery shows that adsorbate-induced superstructures are not limited to special grain boundaries but may exist at a variety of general grain boundaries and hence can impact the performance of polycrystalline engineering alloys.

**One Sentence Summary:** Segregated Bi atoms at general grain boundaries in nickel adopt a variety of superstructures as shown by atomic-resolution STEM.

**Main Text:**

Many properties of polycrystalline metals and ceramics are intimately linked to the structure and composition of their grain boundaries (*1*). Alloying elements, dopants, and impurities are often present at grain boundaries in elevated concentrations compared to grain interiors, an effect known as grain boundary segregation or adsorption. While segregation can enhance macroscopic properties (*2*), it often leads to severe degradation of properties and performance (*3, 4*). Understanding how and why this degradation occurs at the atomic scale is a crucial step toward engineering innovative materials that can resist such deleterious effects.

A recent advance in materials engineering is the discovery that grain boundaries behave in a phase-like manner, transitioning from one state to another as a function of temperature and composition (*5-8*). The term 'complexion' has been introduced to distinguish such interfacial states from bulk phases (*9*). Complexions have been discovered at dislocations (*10*), twin boundaries (*11*), and stacking faults (*12*), and they play a role in nanocrystalline alloys (*13*). However, the exact structural arrangement of adsorbates within complexions and the resultant impact on properties is still largely unknown.

The atomic structure and solute segregation of grain boundaries is often analyzed by transmission electron microscopy (TEM) in ceramics (*2, 14-18*) and metals (*4, 19-21*), and more recently atom probe tomography (APT) has become a useful tool for grain boundaries due to its complementary analytical strengths (*22-24*). However, only a handful of studies have studied the structural arrangement of adsorbates at general grain boundaries in polycrystalline materials, e.g. (*15-18, 20, 21*). Some degree of grain boundary adsorbate periodicity was evident in a few of these studies, e.g. along one side of nanometer-thick intergranular "glassy" films in $Si_3N_4$ (*16-18*), but no evidence of widespread adsorbate-induced grain boundary superstructures has been reported. In contrast to these studies, TEM studies on special high-symmetry boundaries, such as tilt (*2, 4, 14, 19*) and twist (*25*) boundaries in artificial bicrystals often reveal striking, periodic patterns of segregated elements, e.g. in Bi-doped Cu (*4*) and rare earth-doped alumina (*2*). It should also be noted that an interface reconstruction has been observed at a Ni-$Al_2O_3$ phase boundary (*26*).

Unlike the grain boundaries in high-symmetry tilt or twist bicrystals, the majority of grain boundaries in polycrystalline materials are of mixed twist and tilt character. Mixed boundaries are sometimes called "random" or "general" grain boundaries (*27*). The common definition of a general grain boundary is one with a large inverse coincidence ($\Sigma > 29$) (*8*). Although this $\Sigma$-based definition has received criticism (*28*), it is widely used (*29*), so for the purposes of the present work a general boundary is simply one that lacks significant lattice coincidence. General grain boundaries are populous in polycrystalline engineering materials and are often weaker mechanically and chemically than higher-symmetry special grain boundaries, and thereby can limit macroscopic properties and performance. Hence, understanding these performance-limiting grain boundaries is critical to enhance our ability to engineer next-generation materials (*8, 30*).

Our previous work on liquid-metal embrittlement of Ni by Bi showed two Bi-rich layers visible at the grain boundary with linear periodicity (*21*). However, if the segregated adsorbate atoms had superstructures was unclear. Here, we present experimental results from scanning TEM (STEM) and simulated results from density functional theory (DFT) to demonstrate that a variety of periodic

adsorbate superstructures form at naturally occurring, randomly selected general grain boundaries in Bi-infused polycrystalline nickel. We discovered that the grain boundary reconstructions at these boundaries are not driven by the grain boundary misorientation, as commonly believed, but by the crystallographic orientation of the grain boundary plane. In this way, these grain boundary reconstructions are strongly analogous to surface reconstructions, which are also driven by the crystallography of the terminating surface and which alter the two-dimensional translational symmetry of the interface, influencing surface diffusion coefficients (*31*), electronic (*32*), and other physical properties.

## EXPERIMENTAL AND THEORETICAL RESULTS

We randomly selected twelve grain boundaries from a Bi-infused Ni polycrystalline specimen and examined them with aberration-corrected STEM (Fig. S1–S14 and Table S1) (*33*). The Ni-Bi alloy has the equilibrium solidus composition at 700 °C, which we estimated to be Ni – 0.22 at% Bi based on recent CALPHAD data (*34*). The misorientation of all twelve randomly selected grain boundaries was determined via a detailed Kikuchi diffraction pattern analysis. Calculations (*35*) done with this misorientation data showed that eleven of the twelve boundaries were general grain boundaries with Σ values greater than 500 (Table S1). One of the twelve boundaries was determined to be a Σ3 twin boundary. Bi adsorbate superstructures were discovered at many of the general grain boundaries, and the Bi segregation was confirmed by energy-dispersive X-ray spectroscopy (EDS) (Fig. S15).

We employ two different categories of notation to describe the Bi adsorbate superstructures. (i) When discussing the arrangement of Bi atoms within the grain boundary plane, we use Wood's notation (*36*) (e.g., Fig. 1 shows a C(2x2) reconstruction) or matrix notation (*37*) (e.g. Fig. 2 includes results for the [5-511] reconstruction, which cannot be clearly represented by Wood's notation), both common in surface science. (ii) When discussing how the Bi adsorbate atoms appear when viewed from the side in projection (i.e., as in TEM images), we refer to the number of Bi atoms that appear to be sitting on top of a given number of Ni atoms (e.g., Fig. 1B shows a 2Bi/4Ni superstructure, the side view of Fig. 1A parallel to [010]).

We observed the simplest Bi adsorbate pattern of 2Bi/4Ni for the (100) grain boundary facet (Fig. 1 A–D). The (110) grain boundary facet (Fig. 1 E–H) exhibits a 3Bi/6Ni superstructure when viewed from the side parallel to $[1\bar{1}1]$. Both of these superstructures reduce to an apparent 1Bi/2Ni superstructure when viewed from the side, if the primitive repeat unit is considered. Finally, the (111) grain boundary facet (Fig. 1 I–L) exhibits a 10Bi/16Ni superstructure when viewed parallel to $[1\bar{1}0]$, which reduces to a 5Bi/8Ni primitive repeat unit. Additionally, we observed a 5Bi/10Ni superstructure (Fig. S22) on the (111) boundary plane.

The relationship between Bi and Ni visible in the TEM images in Fig. 1 are two-dimensional projections and do not provide the three-dimensional atomic arrangements in the plane of the grain boundary. To address this issue, we conducted DFT calculations of relaxed surface free energies for various low-energy superstructures for the corresponding low-index crystallographic planes (Fig. 2). The atomic models from the DFT calculations form Bi superstructures nearly identical to the experiments when viewed from the side (Fig. 1). We note here that while DFT surface calculations in general may not capture the key features of grain boundaries in other alloys, our previous work (38) has shown that

surface DFT calculations are a reasonable approximation for grain boundaries in Ni-Bi alloys because (i) the total energy of Ni-Bi grain boundaries can be predicted with tolerable accuracy from the energies of the two surfaces alone, and (ii) the Bi-Bi atomic bonds across the Bi-rich bilayer at the grain boundary are relatively weak compared to Bi-Ni bonds on either side of the boundary. This latter point is related to the Bi-rich bilayer at the grain boundary and is demonstrated by the bonding charge distributions illustrated in Fig. 2, which we discuss in more detail below. The atomic models from the calculations form Bi superstructures nearly identical to the experiments when viewed from the side (Fig. 1).

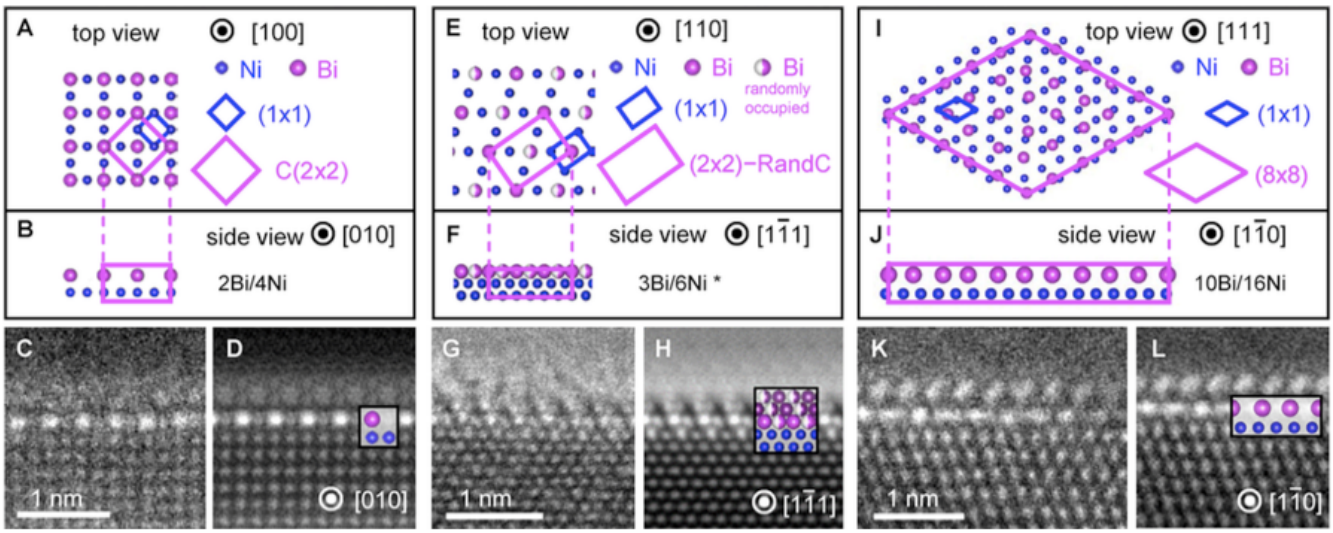


**Fig. 1.** Atomic-scale segregation-induced superstructures in the Ni-Bi system for (100) (A–D), (110) (E–H), and (111) (I–L) crystallographic facets. These crystallographic facets belong to grain boundaries #7, #2, and #5, respectively (Table S1). Atomic-resolution high-angle annular dark field (HAADF) STEM images of Bi-based grain boundary superstructures (original images: C, G, K; wrapped images: D, H, L) show periodic arrangements of Bi atoms that are crystallographically related to the underlying nickel grains. Surface DFT calculations produce Bi-based superstructures (A, E, I) that exhibit the same periodicity as the Bi adsorbate atoms in the HAADF-STEM images (C, D, G, H, K, L) when viewed from the side as two-dimensional projections (B, F, J). HAADF-STEM images (D, H, L) have been wrapped and averaged following the algorithm in Ref. (*39*) to help to determine the exact location of the Bi atoms. (*Note: The 3Bi/6Ni two-dimensional superstructure in panel (F) appears as 3Bi/6Ni when viewed in this direction if the lower-intensity, randomly centered Bi atoms are not counted).

The grain boundaries we analyzed in the experimental images were taken from Bi-saturated Ni specimens in equilibrium with the Bi-rich liquid, as we prepared them under liquid metal embrittlement conditions, though some local variations in Bi chemical potential likely exist due to kinetic factors (*33*). In the case of the (100) and (111) grain boundary facets in Fig. 1, the DFT-calculated surface superstructures (Fig. 1A, I; Fig. S26, S28) correspond to a superstructure that exists in a low energy state for at least one chemical potential (Fig. 2A, C). For the (100) surface, one low-energy superstructure is the C(2x2) surface reconstruction (Fig. S20), as shown in Fig. 1A. For the (111) surface, the (8x8) reconstruction (Fig. S23) is one of the stable reconstructions based on the DFT surface calculations, as shown in Fig. 1I. In addition, the [5-511] structure (Fig. S22) on a Ni (111) surface has comparable energy with the (8x8) reconstruction (Fig. 2C) and is also considered as a stable structure. For the (110) surface (Fig. 1E), DFT calculations show that three different reconstructions (Fig. S21, S27) have similar energy at a chemical potential near the bare Ni surface: The (2x2), C(2x2), and a randomly centered superlattice of C(2x2) we call a (2x2)-RandC. This similarity suggests a superstructure for the (110) surface in which the basic motif is (2x2) with random centering (Fig. 1E), in which atoms that are half white and half magenta represent Bi sites that are randomly occupied. This random occupation of

the centering atoms is consistent with Figs. 1G and 1H, where variable intensity Bi columns contrast with the strong intensity of the other columns. Taken together, we suggest that superstructures in Bi-doped Ni grain boundaries closely resemble surface reconstructions.

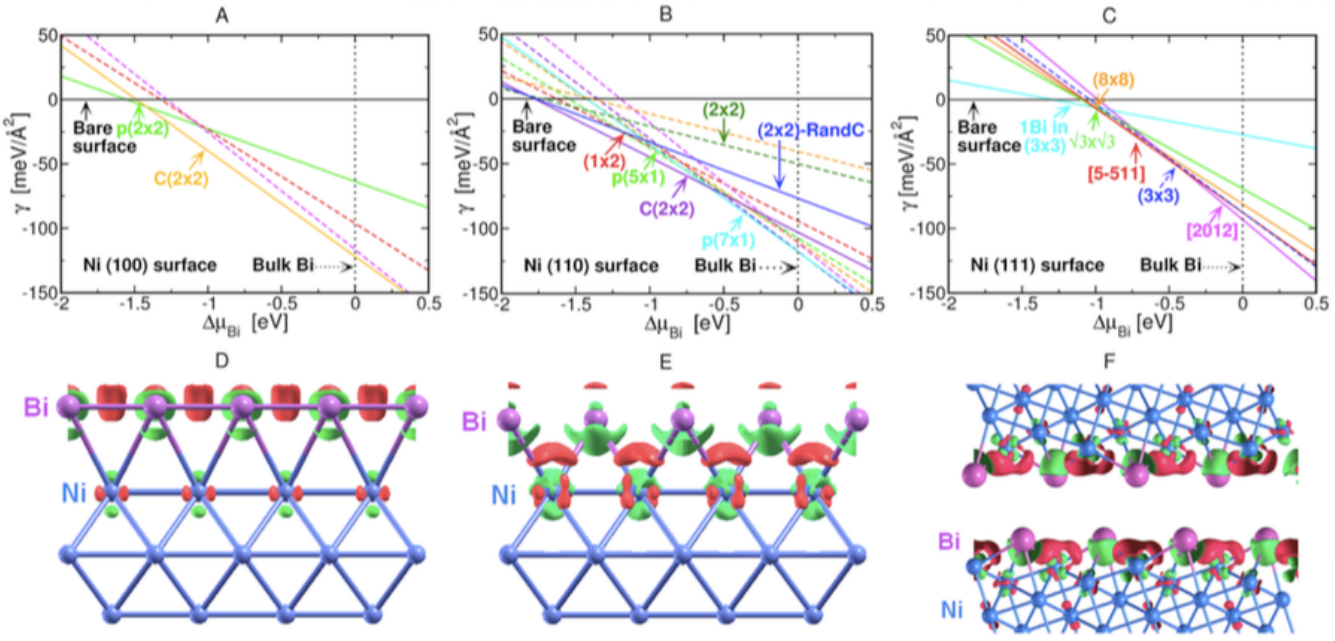


**Fig. 2.** Results of DFT calculations for Ni-Bi free surfaces and a grain boundary. (A–C) DFT calculations of surface free energy as a function of chemical potential for various Bi-based superstructures on three different Ni surfaces: (A) Ni(100) surface, (B) Ni(110) surface, and (C) Ni(111) surface. (D–F) Charge density models based on DFT calculations: (D) Unreconstructed (i.e., (1x1)) Bi monolayer on the Ni(100) surface; (E) C(2x2) superstructure on the Ni (100) surface; (F) Σ5-120 grain boundary. In these charge density models, red indicates increased charge density and green indicates charge depletion.

The surface free energy varies as a function of chemical potential for a series of different Bi-based superstructures based on our DFT calculations (Fig. 2A–C). Charge density figures (Fig. 2D–F) depict the bonding between Ni and Bi atoms for three model superstructures, two at surfaces and one at a grain boundary, in which red indicates increased charge density and green indicates a depletion of charge. Our figures illustrate relaxed surface and grain boundary geometries together with the bonding charge density $\Delta\rho(\mathrm{r})$, defined as

$$\Delta\rho(\mathrm{r}) = \rho_{Tot}^{SC}(\mathrm{r}) - \rho_{Ni}^{SC}(\mathrm{r}) - \rho_{Bi}^{atomic}(\mathrm{r}) \qquad \text{(eq. 1)}$$

Here, $\rho^{SC}$ indicates a self-consistent interacting charge density, while $\rho^{atomic}$ indicates a superposition of isolated atomic charge densities. "Tot", "Ni", and "Bi" refer, respectively, to the complete Bi on Ni structure, the Ni atoms alone, and the Bi atoms alone. Hence, $\Delta\rho$ highlights the charge transfer due to Bi-Ni and Bi-Bi chemical bonding.

Positive $\rho^{SC}$ between atoms (red in Fig. 2D–F) indicates formation of chemical bonds occupied by electrons drawn away from the atoms resulting in negative $\rho^{SC}$ (green in Fig. 2D–F) surrounding the atoms. Fig. 2D shows that on an unreconstructed 1x1 Bi monolayer, the Bi atoms bond to each other but do not bond to the Ni surface. In the C(2x2) structure (Fig. 2E) the atoms bond to the Ni surface but not to each other. The grain boundary charge density figure in Fig. 2F shows the bonding of Bi to the

adjacent Ni surfaces, while the lack of charge density across the boundary suggests a dramatic loss of cohesion (*38, 40*). This result is consistent with the effect of liquid metal embrittlement in this system, which is to dramatically reduce the cohesive strength across the grain boundaries.

General grain boundaries in Bi-infused Ni exhibit a morphology comprised of alternating facets (Fig. 3A). Atomic-resolution images of these facets (Fig. 3B–E) reveal Bi-based superstructures similar to the superstructures in Fig. 1. Two crystal planes, one from each grain, join at each facet to produce the grain boundary. We determined the crystallographic indices of the four marked boundary planes in Fig. 3A by standard electron microscopy methods to be a vicinal (322)/($\bar{1}10$) pair (N1/N2) and a vicinal (101)/($7\bar{9}\bar{5}$) pair (N3/N4). With these results (Fig. S16–S19), we generated an atomic model (Fig. 3F) of the grain boundary in Fig. 3A.

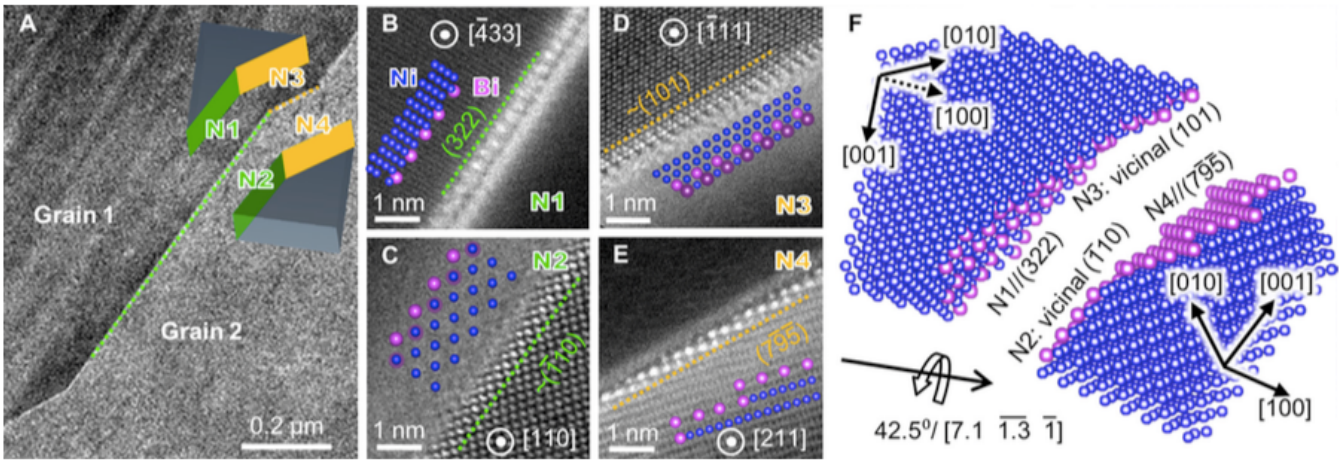


**Fig. 3.** Grain boundary facets in Bi-doped Ni. (A) HAADF-STEM image of a general grain boundary in Bi-doped Ni, which contains micron-sized facets. The grain boundary plane pairs ("grain boundary surfaces") of one facet are marked as N1 and N2 (green) and those of a second facet are marked as N3 and N4 (yellow); (B–E) HAADF-STEM images of the four grain boundary facet planes (with inset atomic diagrams) showing the arrangement of Bi atoms at the grain boundary ((B) N1, (C) N2, (D) N3, (E) N4); (F) Schematic model of the atomic structure of these two grain boundary facets. In this model, the grain boundary is intentionally separated by nanometers to show the grain boundary facet surfaces. These HAADF-STEM images were obtained from grain boundary #2 (Table S1).

The faceting of the grain boundary appears to be driven by the formation of a low-energy crystal plane on one of the adjacent grain surfaces, which is a known energy-lowering mechanism (*41*). Bi segregation to the grain boundary is also an energy-lowering mechanism, and these two mechanisms occur such that the net result is Bi segregation to faceted grain boundaries, some of which contain low-index facets. In the case of the grain boundary in Fig. 3, two of the boundary surfaces happen to be of {110} type (see other cases in Tables S1 and S2). Interestingly, these low-index grain surfaces are only vicinal (Fig. S18–S19) – the grain boundary plane is not exactly parallel to the beam direction when the crystallite itself is on zone axis. In contrast, the high-index surfaces on the opposite side of these boundaries are nearly exactly (322) and ($7\bar{9}\bar{5}$), which consist of {111} terraces separated by single-atom-height steps.

The micro-facets visible in the general grain boundary can be seen on the intergranular fracture surfaces in scanning electron microscope (SEM) images (Fig. S30). These facets are evidence of the well-known faceting transitions (*42, 43*) caused by adsorbed impurities at grain boundaries. Based on atomic-resolution HAADF-STEM imaging of the grain boundary facet surfaces present along the 11 general grain boundaries in this study, containing 27 facets total (Table S1 and Fig. S3–S13), approximately

22% (6 of 27 facets) were terminated by low-index planes and the remaining 78% (21 of 27 facets) were vicinal to low-index planes. Of the 27 facets, we identified superstructures on only 10 facets due to limitations related to STEM imaging and sample geometry. Four such facets were low-index planes and six facets were high-index vicinal planes (Fig. S24–S25, Table S1).

We plotted the crystallographic orientations of the grain boundary facets on a stereographic triangle (Fig. 4A). The stereographic projection is a common graphical method for visualizing crystallographic data (*44*). Here it illustrates that many planes are centered about the 111 and 203 poles of the stereographic projection. Interestingly, the majority of grain boundary surface planes exist along the two edges of the stereographic triangle that run from 001 to 111 and from 001 to 101, demonstrating that these grain boundary surfaces can be produced by pair combinations of these low-index planes (Fig. S25, Table S2).

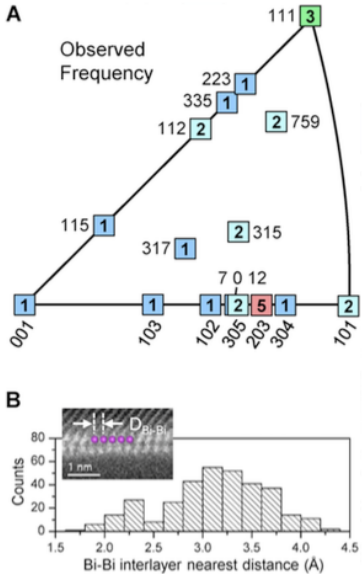


**Fig. 4.** Grain boundary facet orientations and Bi-Bi distances at grain boundaries in Bi-doped Ni. (A) Statistical frequency of grain boundary plane orientations plotted on a stereographic triangle, which includes orientation information for 27 grain boundary facet planes analyzed from 11 general grain boundaries. The number of observations of each plane orientation is represented by a different color square, with the number of observations inscribed inside the square. (B) A histogram of the projected in-plane Bi-Bi distances, showing a peak around 3.0 to 3.5 Å, which is between the first and second nearest neighbor Bi-Bi bond length in Bi metal.

The Bi-Bi atomic spacing in these adsorbate superstructures is large relative to the distances between Ni atoms (Fig. 4B). Because we determined these Bi-Bi distances from STEM images, they could be shorter as they are projected distances. Nevertheless, our histogram indicates a ~3.25 Å lateral spacing between Bi atoms, which sits between the first (3.07 Å) and the second (3.53 Å) Bi-Bi nearest neighbor distances in pure Bi metals (*45*). Furthermore, the lateral Bi-Bi distances do not match the Ni-Ni atomic distances (1.74 Å on (100) planes; 2.10 Å on (110) and (111) planes) in pure Ni. The minimization of strain energy from the large atomic size and bonding length mismatch from the pure metals is a reasonable explanation for the formation of the Bi superstructures at the grain boundaries.

Although the primary effect of these Ni-Bi grain boundary superstructures is the embrittlement of the metal, grain boundary superstructures could potentially play a role in electronic, magnetic, and

diffusion-related properties as well. It is already known that dopant-based grain boundary complexions can change the electrical resistivity of thick-film resistors (*46*) and the coercivity of Nd-Fe-B magnets (*47*), and could affect the giant spin Hall effect in the Cu-Bi system (*48*). If the complexions in these systems form ordered superstructures, the change of two-dimensional translational symmetry at the grain boundaries would impact related physical properties. Moreover, drawing an analogy to the well-known diffusion anisotropy that occurs on reconstructed metal surfaces (*49*), diffusion through superstructures at grain boundaries will likely be anisotropic, and this behavior could potentially be exploited to engineer anisotropic microstructures with enhanced properties.

The discovery of Bi segregation-induced superstructures at general grain boundaries greatly enriches our limited knowledge of the atomic structure of complexions and may offer new insights into a spectrum of structure-related grain boundary properties such as plasticity, diffusivity, and conductivity. We suggest that ordered grain boundary superstructures may indeed be a general, although not necessarily universal, feature of polycrystalline materials. This suggestion is based on an analogy to the reconstruction behavior of free surfaces, in which adsorbates often form periodic structures, e.g. Bi on Cu (*50*), but can also form disordered overlayers, e.g. S on Cu (*51*). Additional studies using TEM and complementary techniques such as APT are needed to determine if segregation-induced grain boundary superstructures exist in other polycrystalline metals, especially in systems with strong attractive adsorbate-metal pair interactions.

## References and Notes:


1. A. P. Sutton, R. W. Baluffi, *Interfaces in Crystalline Materials*. (Oxford University Press, New York, 1995).
2. J. P. Buban *et al.*, Grain boundary strengthening in alumina by rare earth impurities. *Science* **311**, 212–215 (2006).
3. M. Yamaguchi, M. Shiga, H. Kaburaki, Grain boundary decohesion by impurity segregation in a nickel-sulfur system. *Science* **307**, 393–397 (2005).
4. G. Duscher, M. F. Chisholm, U. Alber, M. Rühle, Bismuth-induced embrittlement of copper grain boundaries. *Nature Materials* **3**, 621–626 (2004).
5. S. J. Dillon, M. Tang, W. C. Carter, M. P. Harmer, Complexion: A new concept for kinetic engineering in materials science. *Acta Materialia* **55**, 6208–6218 (2007).
6. P. R. Cantwell *et al.*, Grain boundary complexions. *Acta Materialia* **62**, 1–48 (2014).
7. M. P. Harmer, The phase behavior of interfaces. *Science* **332**, 182–183 (2011).
8. T. Watanabe, Grain boundary engineering: Historical perspective and future prospects. *Journal of Materials Science* **46**, 4095–4115 (2011).
9. M. Tang, W. C. Carter, R. M. Cannon, Diffuse interface model for structural transitions of grain boundaries. *Physical Review B* **73**, 024102 (2006).
10. M. Kuzmina, M. Herbig, D. Ponge, S. Sandlöbes, D. Raabe, Linear complexions: Confined chemical and structural states at dislocations. *Science* **349**, 1080–1083 (2015).
11. J. F. Nie, Y. M. Zhu, J. Z. Liu, X. Y. Fang, Periodic segregation of solute atoms in fully coherent twin boundaries. *Science* **340**, 957–960 (2013).
12. T. M. Smith *et al.*, Phase transformation strengthening of high-temperature superalloys. *Nature Communications* **7**, 13434 (2016).
13. T. J. Rupert, The role of complexions in metallic nano-grain stability and deformation. *Current Opinion in Solid State and Materials Science* **20**, 257–267 (2016).
14. R. F. Klie, N. D. Browning, Atomic scale characterization of oxygen vacancy segregation at $SrTiO_3$ grain boundaries. *Applied Physics Letters* **77**, 3737–3739 (2000).
15. Z. Yu, Q. Wu, J. M. Rickman, H. M. Chan, M. P. Harmer, Atomic-resolution observation of Hf-doped alumina grain boundaries. *Scripta Materialia* **68**, 703–706 (2013).
16. N. Shibata *et al.*, Observation of rare-earth segregation in silicon nitride ceramics at subnanometre dimensions. *Nature* **428**, 730–733 (2004).

17. A. Ziegler *et al.*, Interface structure and atomic bonding characteristics in silicon nitride ceramics. *Science* **306**, 1768–1770 (2004).
18. G. B. Winkelman *et al.*, Three-dimensional organization of rare-earth atoms at grain boundaries in silicon nitride. *Applied Physics Letters* **87**, 061911 (2005).
19. U. Alber, H. Müllejans, M. Rühle, Bismuth segregation at copper grain boundaries. *Acta Materialia* **47**, 4047–4060 (1999).
20. A. Kundu, K. M. Asl, J. Luo, M. P. Harmer, Identification of a bilayer grain boundary complexion in Bi-doped Cu. *Scripta Materialia* **68**, 146–149 (2013).
21. J. Luo, H. Cheng, K. M. Asl, C. J. Kiely, M. P. Harmer, The role of a bilayer interfacial phase on liquid metal embrittlement. *Science* **333**, 1730–1733 (2011).
22. L. Yao, S. Ringer, J. Cairney, M. K. Miller, The anatomy of grain boundaries: Their structure and atomic-level solute distribution. *Scripta Materialia* **69**, 622-625 (2013).
23. M. Herbig *et al.*, Atomic-scale quantification of grain boundary segregation in nanocrystalline material. *Physical Review Letters* **112**, 126103 (2014).
24. J. Hu, Y. Shi, X. Sauvage, G. Sha, K. Lu, Grain boundary stability governs hardening and softening in extremely fine nanograined metals. *Science* **355**, 1292-1296 (2017).
25. S. Ma *et al.*, A grain boundary phase transition in Si–Au. *Scripta Materialia* **66**, 203–206 (2012).
26. H. Meltzman, D. Mordehai, W. D. Kaplan, Solid–solid interface reconstruction at equilibrated Ni–$Al_2O_3$ interfaces. *Acta Materialia* **60**, 4359–4369 (2012).
27. A. Morawiec, K. Glowinski, On "macroscopic" characterization of mixed grain boundaries. *Acta Materialia* **61**, 5756–5767 (2013).
28. V. Randle, The coincidence site lattice and the 'sigma enigma'. *Materials Characterization* **47**, 411-416 (2001).
29. L. Priester, *Grain boundaries: from theory to engineering*. (Springer Science & Business Media, 2012), vol. 172.
30. P. R. Cantwell, S. Ma, S. A. Bojarski, G. S. Rohrer, M. P. Harmer, Expanding time–temperature-transformation (TTT) diagrams to interfaces: A new approach for grain boundary engineering. *Acta Materialia* **106**, 78–86 (2016).
31. R. Gomer, Diffusion of adsorbates on metal surfaces. *Reports on Progress in Physics* **53**, 917 (1990).
32. I.-W. Lyo, E. Kaxiras, P. Avouris, Adsorption of boron on Si (111): Its effect on surface electronic states and reconstruction. *Physical Review Letters* **63**, 1261 (1989).
33. Materials and methods are available as supplementary materials at the Science website.
34. J. Wang, F.-g. Meng, L.-b. Liu, Z. Jin, Thermodynamic optimization of the Bi-Ni binary system. *Transactions of Nonferrous Metals Society of China* **21**, 139-145 (2011).
35. K. Glowinski, A. Morawiec, "A toolbox for geometric grain boundary characterization," *Proceedings of the 1st International Conference on 3D Materials Science* (Springer International Publishing, 2012).
36. E. A. Wood, Vocabulary of Surface Crystallography. *Journal of Applied Physics* **35**, 1306-1312 (1964).
37. K. Oura, V. G. Lifshits, A. A. Saranin, A. V. Zotov, M. Katayama, *Surface Science: An Introduction*. (Springer, Berlin, 2003).
38. Q. Gao, M. Widom, First-principles study of bismuth films at transition-metal grain boundaries. *Physical Review B* **90**, 144102 (2014).
39. A. Kirkland, W. Saxton, Cation segregation in $Nb_{16}W_{18}O_{94}$ using high angle annular dark field scanning transmission electron microscopy and image processing. *Journal of Microscopy* **206**, 1–6 (2002).
40. Q. Gao, M. Widom, Surface and grain boundary complexions in transition metal–bismuth alloys. *Current Opinion in Solid State and Materials Science* **20**, 240–246 (2016).
41. G. S. Rohrer *et al.*, The distribution of internal interfaces in polycrystals. *Zeitschrift für Metallkunde* **95**, 197-214 (2004).
42. M. Menyhard, B. Blum, C. McMahon, Grain boundary segregation and transformations in Bi-doped polycrystalline copper. *Acta Metallurgica* **37**, 549–557 (1989).
43. T. Ference, R. Balluffi, Observation of a reversible grain boundary faceting transition induced by changes of composition. *Scripta Metallurgica* **22**, 1929–1934 (1988).
44. M. De Graef, M. E. McHenry, *Structure of materials: an introduction to crystallography, diffraction and symmetry*. (Cambridge University Press, 2012).
45. P. Cucka, C. Barrett, The crystal structure of Bi and of solid solutions of Pb, Sn, Sb and Te in Bi. *Acta Crystallographica* **15**, 865–872 (1962).
46. Y.-M. Chiang, L. A. Silverman, R. H. French, R. M. Cannon, Thin glass film between ultrafine conductor particles in thick-film resistors. *Journal of the American Ceramic Society* **77**, 1143-1152 (1994).
47. O. Gutfleisch *et al.*, Magnetic materials and devices for the 21st century: Stronger, lighter, and more energy efficient. *Advanced Materials* **23**, 821-842 (2011).

48. D. V. Federov *et al.*, Analysis of the giant spin Hall effect in Cu(Bi) alloys. *Physical Review B* **88**, 085116 (2013).
49. G. Antczak, G. Ehrlich, Jump processes in surface diffusion. *Surface Science Reports* **62**, 39-61 (2007).
50. F. Delamare, G. Rhead, First stages of the deposition of bismuth on copper examined by LEED: I. The (100) substrate. *Surface Science* **35**, 172–184 (1973).
51. G. B. D. Rousseau *et al.*, A structural study of disordered sulfur overlayers on Cu(111). *Surface Science* **600**, 897-903 (2006).
52. C. Young, J. Steele, J. Lytton, Characterization of bicrystals using Kikuchi patterns. *Metallurgical Transactions* **4**, 2081–2089 (1973).
53. Q. Gao, M. Widom, First-principles study of bismuth films on the Ni(111) surface. *Physical Review B* **88**, 155416 (2013).
54. P. E. Blöchl, Projector augmented-wave method. *Physical Review B* **50**, 17953 (1994).
55. J. P. Perdew, K. Burke, M. Ernzerhof, Generalized gradient approximation made simple. *Physical Review Letters* **77**, 3865–3868 (1996).
56. G. Kresse, J. Hafner, *Ab initio* molecular dynamics for liquid metals. *Physical Review B* **47**, 558–561 (1993).
57. G. Kresse, J. Furthmüller, Efficient iterative schemes for *ab initio* total-energy calculations using a plane-wave basis set. *Physical review B* **54**, 11169 (1996).
58. W. Clendening, C. T. Campbell, The growth modes of vapor-deposited bismuth on a Cu(110) surface. *The Journal of Chemical Physics* **90**, 6656–6663 (1989).
59. T. R. Bollmann, R. van Gastel, H. J. Zandvliet, B. Poelsema, Quantum size effect driven structure modifications of Bi films on Ni(111). *Physical Review Letters* **107**, 176102 (2011).
60. T. R. Bollmann, R. van Gastel, H. J. Zandvliet, B. Poelsema, Erratum: Quantum Size Effect Driven Structure Modifications of Bi Films on Ni(111). *Physical Review Letters* **109**, 269903 (2012).
61. D. Kaminski, P. Poodt, E. Aret, N. Radenovic, E. Vlieg, Surface alloys, overlayer and incommensurate structures of Bi on Cu(111). *Surface Science* **575**, 233–246 (2005).

**Acknowledgments:** Additional data and images are available in the Supplementary Materials (SM) at the Science website. We would like to thank Professor Wenzheng Zhang (School of Materials Science & Engineering, Tsinghua University) and Dr. Xinfu Gu (School of Materials Science and Engineering, University of Science and Technology Beijing) for valuable discussions. The authors gratefully acknowledge support from the ONR-MURI program (grant no. N00014-11-0678). Partial support for work at CMU was provided by the Department of Energy grant DE-SC0014506.

**Supplementary Materials:**

Materials and Methods
Supplementary Text
Figs. S1–S30
Tables S1–S2
References (*52–61*)


# Supplementary Materials for

## Segregation-induced ordered superstructures at general grain boundaries in metals

Zhiyang Yu, Patrick R. Cantwell, Qin Gao, Denise Yin, Yuanyao Zhang, Naixie Zhou, Gregory S. Rohrer, Michael Widom, Jian Luo, Martin P. Harmer

Correspondence to: mph2@lehigh.edu (M.P.H.) and jluo@alum.mit.edu (J.L.)

**This PDF file includes:**

## Materials and Methods

Nickel foil (99.9945%), Bi powder, and Ni powder were purchased from Alfa Aesar. A mixture of Bi and Ni powders with a liquidus composition of 26.5 at.% Ni was placed on top of Ni foil and annealed isothermally at 700 °C for 5 hours in a tube furnace with flowing Ar - 5% $H_2$ gas. Water quenching was applied in order to preserve the high temperature structure. The quenched specimens were sectioned and polished. Specimens were prepared for STEM via the liftout method using a dual-beam Focused Ion Beam/Scanning Electron Microscope (FIB/SEM; Fig. S1). In order to obtain a variety of general grain boundaries, we selected the grain boundaries for this study at random (without prior knowledge of their crystallography) from a region approximately 10 to 20 μm from the Bi penetration front (Fig. S1). Grain boundaries with evident grooves were randomly selected and lifted out from this region to produce the TEM samples. After thinning in the FIB/SEM (FEI Scios DualBeam) using a 5 kV ion beam, the thin slabs were carefully milled with low energy Ar (0.5 kV) ions (Fischione Model 1040) to reduce surface damage. After final milling, the TEM samples were approximately 30 to 60 nm thick (Fig. S1C). Twelve TEM samples were prepared using the FIB liftout method. Only one FIB sample contained a twin boundary; the other eleven samples were general grain boundaries. The configurations of Bi atoms within the 12 boundaries were carefully explored using an aberration corrected scanning transmission electron microscope (STEM, JEOL 200CF) under high angle annular dark field (HAADF) mode. The relatively large collection angle (70–200 mrad) of the HAADF detector enables the acquisition of atomic structure images with excellent atomic-number (Z) sensitivity.

## Supplementary Text

(I) Identification of the normal of the boundary planes

Grain boundary plane normals were identified using two methods: the Kikuchi pattern method (Fig. S2A–B)) and the two-dimensional lattice imaging method (Fig. S2C). The Kikuchi pattern method was applied most often. When the boundaries were aligned to edge-on conditions (Fig. S2A), in most cases, the grains were aligned on high Miller index zone axes (Fig. S2B). The {320} Kikuchi bands were parallel to the boundary planes and thus they were assigned the indices of the boundary plane of the right grain. Likewise, the normal of the boundary plane of the left grain could be identified when the left grain was aligned to a known axis with the boundary edge-on. Occasionally, the grain boundary of interest was set to an edge-on condition with one of the two adjoining grains aligned to a low Miller index zone axis. Under this condition (Fig. S2C), the mean boundary plane could be identified as a {12 7 0} plane using the two orthogonal (100) and (010) lattice fringes as references.

On the basis of the two aforementioned methods, the Miller indices of the grain boundary planes of the 12 TEM samples were identified in Fig. 1, Fig. 3 and Fig. S3–S14. The results are summarized in Table S1. We also estimate the errors of the boundary indices in Table S1. The errors must be included for two reasons. First, some boundary planes contained atomic-scale steps through a limited sample thickness (usually 30–60nm). A typical example is shown in Fig. S18. As one can see there, the presence of steps gives rise to errors. Second, there are a very limited numbers of high Miller index conditions if the boundary is aligned edge-on. For example, when the grain boundary was set to an edge-on condition (close to the [156] axis, Fig. S3B), we cannot find a rational Kikuchi band in parallel with the boundary plane (Fig. S3C); when we aligned the grain boundary slightly off the edge-on condition ([134] axis, Fig. S3C), {531} Kikuchi bands in parallel with the N1 boundary plane started to emerge.

Further through-focal images (Fig. S3 E–H) indicate the existence of {531} terraces along the beam direction. Because the [156] axis (edge-on condition) was ~ 5° off the [134] axis, it is reasonable to treat 5° as the deviation from the actual N1 boundary plane (of the left grain) to the identified $\{5\bar{3}1\}$ facets. The errors were given in the brackets after the Miller indices of the boundary planes in Fig. S2–S14 and Table S1. As one can see in Table S1, the errors were just a few degrees and we believe those indices were close to the actual boundary planes where Bi atoms were adsorbed.

In general, typical Ni(Bi) grain boundaries show alternate facets which repeat one after the other for several microns (samples #2 through #12). Thus, four sets of grain boundary planes are required to be identified for a typical Ni(Bi) boundary. The four boundary planes consist of 2 DOFs (degree of freedom) of the boundary. Sample #1 did not show alternate faceting in the cross-section and only two sets of boundary plane were identified. The misorientation matrices of samples #1 though #5 were determined on a basis of a standard Kikuchi pattern analysis method (*52*) (Fig. S16, Section II). All five DOFs are thus derived for a Ni(Bi) boundary for samples #1 through #5. In samples #6 through #12, we determined a fraction of the four boundary planes.

The grain boundary superstructures observed in this study are continuous and uniform throughout the TEM specimen thickness (approximately 30 to 60 nm thick, depending on the sample). We carefully checked for this structural continuity via through-focal series imaging in the STEM (e.g., Fig. S17–S19), which demonstrated that the observed Bi superstructures did not change as the objective lens defocus was varied.

(II) Identification of the misorientation parameters Ni(Bi) boundaries

The misorientation parameters of two Ni crystals were established using Kikuchi patterns from the two grains. Basically, for each grain, according to Young's procedure (*52*), three orthogonal frames must be established (Fig. S16), which are:

1) The crystal frame (*CF*),
2) The Kikuchi pattern frame (*PF*) and
3) The reference (screen) frame (*RF*).

In brief, the first step is to formulate a matrix [*CP*] transforming *CF* to *PF* for each crystal; followed by the establishment of the matrix [*PR*] which represents the rotation of *PF* to *RF*; finally, a matrix representing the rotation of *CF* to *RF* is given by

$$[CR] = [CP][PR] \qquad [1].$$

Finally, the misorientation matrix which represents the orientation relationship between the two interested grains is given by

$$[M12] = [CR2]^{-1}[CR1] = [PR2]^{-1}[CP2]^{-1}[CP1][PR1] \qquad [2].$$

On the basis of the Kikuchi patterns shown in Fig. S16 and by following the procedures given in (*52*), the misorientation matrix of sample #2 is then derived as

$$\begin{pmatrix} -0.0473 & -0.7452 & -0.6652 \\ 0.9865 & -0.1392 & 0.0858 \\ -0.1565 & -0.6521 & 0.7418 \end{pmatrix}.$$

Its angle/axis representation is 102.84°/[-1.45, -1, 3.40]. We apply the 24 rotational symmetry operations (symmetry of FCC systems) and the minimum rotation angle is 42.54° with a rotation axis of [-7.06, 1.30, 1]. The misorientation matrix with the minimum rotation angle is

$$\begin{pmatrix} 0.9865 & -0.1392 & 0.0858 \\ 0.0473 & 0.7452 & 0.6652 \\ -0.1565 & -0.6521 & 0.7418 \end{pmatrix}.$$

(III) Atomic modeling of Ni(Bi) high-angle grain boundaries

The atomic structures of Ni(Bi) high-angle grain boundaries (Fig. 3F) were retrieved by the following procedures. Here we use sample #2 as an example. The first step is to establish the misorientation matrix (Section II) and the four boundary planes (as shown in Fig, 3: N1 as a (322) plane; N4 as a $(7\bar{9}\bar{5})$ plane; N2 and N3 as vicinal {110} planes). It should be noted that the N1 facet is straight without atomic-scale steps. The N4 facet is quite close to being a $(7\bar{9}\bar{5})$ facet (Fig. S17). The N2 (Fig. S18) and N3 (Fig. S19) boundary planes are vicinal {110} planes, with nearly periodic steps along the electron beam direction. The boundary planes of N2 and N3 could be estimated by the following formula since N1 and N4 are straight planes:

$N2 = M12*N1$ [3]
$N3 = M12^{-1}*N4$ [4].

The Miller index of the N2 facet is approximately $(\,\overline{51}\ 49\ \bar{5}\,)$ and that of the N3 facet is approximately (12 1 13). From the Miller indices, it is clear that these two boundary planes are vicinal.

The second step involves the creation of the two crystals terminated by the four observed boundary planes, with Bi superstructures overlaid on top. The third step is to apply the misorientation matrix and put the two crystals in the same coordinate system. The two crystals are intentionally shifted by approximately 1 to 2 nm to highlight the grain boundary structures (Fig. 3F).

(IV) Assignment of Bi superstructures on low-index grain surfaces

a) Ni(100)–C(2x2)-Bi superstructure

Fig. S20A is the raw HAADF-STEM image of the C(2x2) Bi superstructure (Fig. 1C–D). As shown in the BF-STEM image (Fig. S20B), the nickel lattice does not terminate at the first Bi layer ($L_{Bi1}$; yellow arrow) but extends for another 2 nm (white arrow). This implies that the interface (near the first Bi layer) contains some rough steps. It is not a perfectly straight facet. Actually, there is another short Bi layer ($L_{Bi2}$; red arrow) as suggested by HAADF-STEM imaging (Fig. S20A).

Despite of the existence of rough steps that might complicate the image interpretation, in general there appears to be some extra HAADF-STEM intensity (Fig. S20A, denoted by blue dotted circles) in the middle of every two bright Bi columns. Those columns have HAADF-STEM intensities comparable with those of Ni columns, as shown in the warped image (Fig. 1D). Two different models might lead to the described image feature. In model I, there are no Ni atoms in the Bi layer. The extra HAADF-STEM intensity could possibly arise from the underlying Ni lattice if we recall the fact that (100) boundary planes are slightly rough (Fig. S20B). In model II, Bi and Ni atoms are intermixed and form surface alloys at the interface, as schematically shown in Fig. S20D.

We conducted surface density function theory (DFT) calculations on model I and the model II. First principle calculations suggest that model I with the C(2x2) Bi superstructure is stable and the surface alloy model (model II) is unstable. Hence, we assign this structure as a C(2x2) superstructure on Ni(100).

b) Ni(110)–(2x2)-RandC Bi superstructure

Fig. S21A shows four typical atomic models of Bi superstructures on (110) planes considered by DFT calculations (Fig. S27). Those models retain the symmetry of (110) planes and might produce structures that appear similar when viewed from the side in 2D projection. Along the [111] direction (lower panel of Fig. S21A), (1x2), (2x2)-RandC, and (2x2) models could give rise to 3Bi/6Ni superstructures when viewed in this particular 2D projection. The (2x2)-RandC structure is a randomly centered superlattice of C(2x2), in which every other cell contains a centered Bi atom on average. The C(2x2) model does not match the HAADF-STEM observation in Fig. S21B. Now we consider the HAADF image feature in Fig. S21B. The complicated tri-layer contrast arises from the presence of atomic steps on {110} planes, as confirmed by our through-focal HAADF imaging (Fig. S19). What is more, the columns between every two bright Bi columns produce HAADF intensities that are lower than those of Bi columns but are a bit higher than those of the nearby Ni lattice. If we look at the (1x2) and the (2x2) models, neither Bi atoms nor nickel atoms sit in between the bright Bi columns. As a result, the HAADF intensities in between the bright Bi columns should be lower than those from the Ni lattice. However, this is inconsistent the experimental HAADF-STEM observation. The (2x2)-RandC model has Bi atoms randomly centered, such that they appear on average in every second (2x2) cell. This configuration could give rise to the image feature discussed above. Furthermore, DFT calculations (Fig. S27) suggest that the (2x2)-RandC model has considerably low energy at a certain range of chemical potentials (Fig. 2B). In contrast, the (1x2) and the (2x2) models are not stable (Fig. 2B). Taking all the factors together, it is reasonable to assign the Bi-rich complexion on the Ni(110) grain surface as a (2x2)-RandC superstructure.

c) Ni(111)–[5-511] Bi superstructure

Fig. S22B shows the HAADF-STEM image of a (111) boundary plane with an evident Bi superstructure. Several different atomic configurations of Bi superstructures on (111) surface are examined by DFT calculations (Section VII, Fig. S28). Only the [5-511] Bi superstructure (Fig. S22A) can produce the HAADF-STEM image features in Fig. S22B. Surface DFT calculations reveal that the [5-511] Bi superstructure has a considerably low energy (Fig. 2C). Therefore, we assign this Bi-rich boundary complexion as a [5-511] Bi superstructure.

d) Ni(111)–(8x8) Bi superstructure

Fig. S23B shows the raw HAADF-STEM image of a (111) boundary plane, which has an apparent 10Bi/16Ni superstructure when viewed from the side as a two-dimensional projection (Fig. 2K–L). Several different atomic configurations of Bi superstructures on (111) surfaces are examined by DFT (Section VII, Fig. S28). Only the (8x8) Bi superstructure (Fig. S23A) could produce the HAADF image features in Fig. S23B. Surface DFT calculations reveal that the (8x8) Bi superstructure has a low energy. Therefore, we assign this Bi-rich boundary complexion as an (8x8) superstructure.

(V) More evidence of Bi superstructures on high-index planes

Owing to limited tilt angles accessible in the STEM, the grain boundary planes often could only be aligned to edge-on conditions under high Miller index zone axes. Those orientations might not be suitable for the observation of Bi superstructures. Despite this limitation, we still were able to identify some Bi superstructures. Some typical examples are shown in Fig. S24. The upper panels of Fig. S24 display experimental HAADF-STEM images, with line profiles (lower panels) taken along Bi-rich interfaces and the nearby Ni lattices. The line profiles confirm the presence of one 3Bi/7Ni superstructure (Fig. S24A), two 1Bi/2Ni superstructures (Fig. S24B–C) and one 1Bi/3Ni (Fig. S24D) superstructures.

Occasionally, the high Miller index boundary planes were viewed in suitable conditions and their atomic configurations could thus be revealed (Fig. S25). In Fig. S25A, a (12 7 0) stepped grain surface is dissociated into a (740) and a (530) segment (see section VI). Interestingly, those two segments are decomposed into (110) and (210) structural units. Fig. S25B shows an example of how a high Miller index $(7\bar{9}\bar{5})$ boundary plane is dissociated into (111) and (110) structural units.

In some cases, a Bi superstructure was observed on one grain surface of a particular facet, but not on the opposing surface (e.g., grain boundary #2 in Table S1 has a reconstruction on grain surface N1, which is marked with an 'R', but not on the opposing grain surface N2). We believe the most likely reason for the lack of an observable superstructure on the opposing grain surface is the inability to tilt the sample in the STEM to a favorable orientation for elucidating the superstructure, due to the limited range of tilt angles accessible in the STEM. However, the possibility that there are indeed some instances in which a superstructure exists on one grain surface but not the other cannot be ruled out.

(VI) Structural units of the high-index boundary planes

Interestingly, we found the high Miller index boundary planes (Table S1) in this study could be described as the combination of some structural units ({100}, {110}, {111} and {210}, Table S2). For example, the {795} plane consist of {111} terraces, seven atoms wide, separated by {110} steps with single-atom-height. Thus, {111} and {110} planes serve as the structural units. It is possible that those low Miller index structural units ({100}, {110}, {111} and {210}) have relatively low energies and the dissociation of boundary planes into low Miller index structural units could help to reduce the overall grain boundary energy.

(VII) DFT calculation of Bi superstructures

We conducted density functional theory calculations to study the stabilities of proposed Bi structures on Ni boundary planes. Since the Bi-Bi inter-layer interaction is weak, the stability of the Bi monolayer film at one side of the grain boundary plane is similar as on the surface (*39, 40*). We thus studied the stabilities of Bi monolayer films at some representative Ni surfaces ((111), (110), (100) and (530)). Our calculation methods are similar to our previous study of Bi films on Ni(111) (*53*) , namely PAW potentials (*54*) in the PBE (*55*) generalized gradient approximation with default energy cutoffs using VASP (*56, 57*).

For the Ni (111), (110) and (100) surfaces, we calculated structures proposed from earlier Bi-Ni or Bi-Cu surface experiments (*58-61*). We also proposed structures based on our own HAADF-STEM experiments. Some other trial structures with reasonable Bi-Bi separations were also taken into consideration. For the Ni (530) surface, no surface experiments have been reported. In the calculations, we constructed models with Ni slabs (4, 4, 3, and 20 layers for (111), (110), (100) and (530) respectively) normal to the surface with Bi films on one side. Our cells included 22 Å of vacuum, with periodic boundary conditions. We fixed the in-plane lattice constant to the relaxed bulk Ni lattice constant $a$ = 3.49 Å and fixed the bottom layer Ni atoms at their bulk Ni positions.

To compare the stabilities of Bi structures on the Ni surfaces, we calculated the surface free energies as defined in reference (*39*). From equilibrium thermodynamics, the most stable structure should have a minimum the surface free energy at a certain Bi chemical potential:

$$\gamma = \left[E_{tot} - E_{Ni}^{slab} - E_{Bi}^{bulk} N_{Bi} - \Delta\mu_{Bi} N_{Bi}\right]/\mathrm{A}, \qquad [5]$$

where $E_{tot}$ is the total energy of $N_{Bi}$ atoms of Bi on the surface of the Ni slab, $E_{Ni}^{slab}$ is the energy of the Ni slab with two free surfaces, each of area $A$, $E_{Bi}^{bulk}$ is the bulk Bi energy, and $\Delta\mu_{Bi}$ is the Bi chemical potential relative to bulk Bi.

The results in Fig. S26–29 show the selected calculated structures and surface free energies of Bi on Ni (100), (110), (111) and (530) surfaces respectively. These figures confirm the stability of most of the Bi structures proposed from our grain boundary observations, namely [5-511] on Ni(111) (Fig. S22), (2x2)-RandC (Fig. S21) on Ni(110), C(2x2) on Ni(100) (Fig. S20) and a reconstructed structure on Ni(530) (Fig. S25). The (8x8) structure (Fig. S23) on a Ni(111) surface has comparable energy with the Ni(111)–[5-511] structure.

Our theoretical results also agree well with the earlier surface experiments. The almost stable Bi (8x8) structure was observed on the Ni(111) surface (*59, 60*). In this study, we find that the Bi [2012] structure observed on the Cu (111) surface (*61*) is also stable on the Ni (111) surface. On the Ni(110) surface, the p(5x1) and p(7x1) structures are stable, which were observed on Cu(110) (*58*). On Ni(100), the p(2x2) and C(2x2) structures are stable, which were observed on the Cu(100) surface (*50*).

(VIII) Calculation of Coincident Site Lattice (CSL) ∑ values from misorientation data

Using the misorientation data derived from Kikuchi diffraction pattern analysis (Table S1), we calculated ∑ values for all twelve grain boundary samples in this study using grain boundary calculation software (*35*). The limit misorientation for low-angle boundaries was chosen to be $\omega_0 = 8°$, and an exponent of $p = 0.5$ was used, which are typical values for these parameters (*29*). These parameters were applied using the criterion $\Delta\omega = \omega_0\Sigma^{-p}$ to determine the critical value of allowable angular deviation from exact coincidence, $\Delta\omega$. Using this criterion, eleven of the grain boundaries (#1 through #11 in Table S1) were found to have ∑ values greater than 500 (the upper limit at which the software will calculate a ∑ value), and grain boundary #12 was confirmed to be a ∑3 boundary.

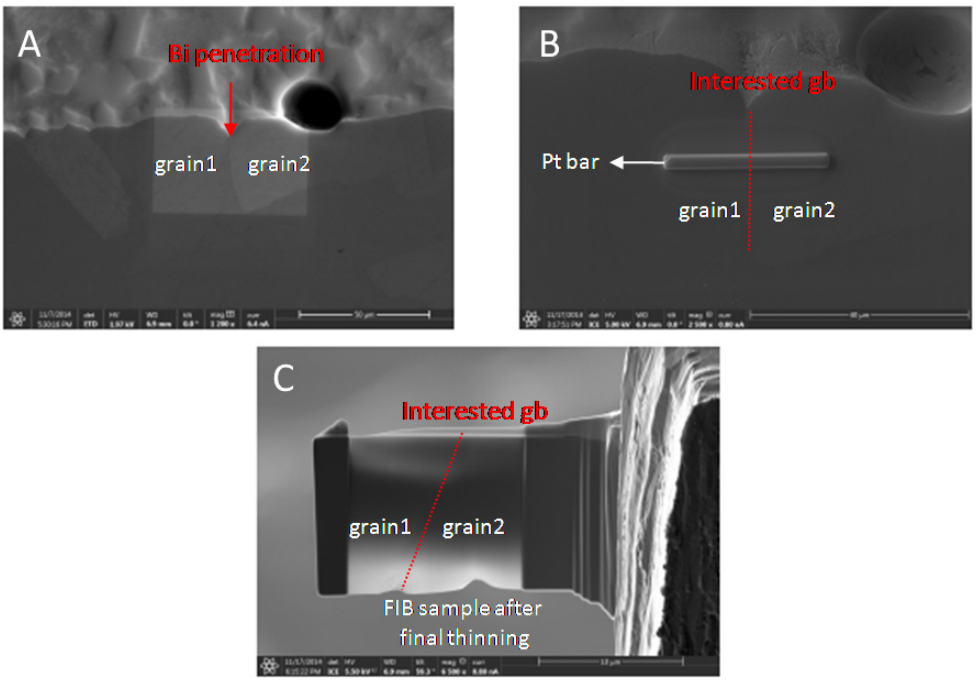


**Fig. S1**

Low magnification scanning electron microscope (SEM) images showing (A, B) the FIB lift-out region. (C) The lift-out sample was attached to a Mo grid and carefully polished to a thickness of approximately 30 to 60nm.

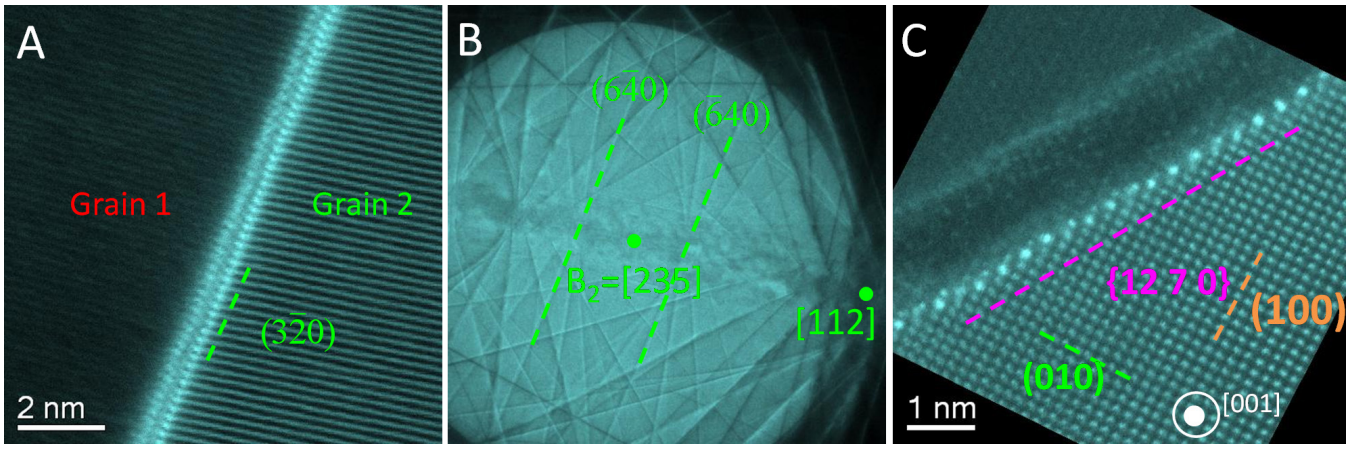


**Fig. S2**

An example of the identification procedure using the Kikuchi pattern method. (A) The boundary was aligned to an edge-on condition using the HAADF image, with the right grain aligned to a known high Miller index zone axis as shown in (B) ([235] axis). (C) Identification of the normal of the boundary plane via the two-dimensional lattice imaging method. The lower grain was aligned to the [001] zone axis.

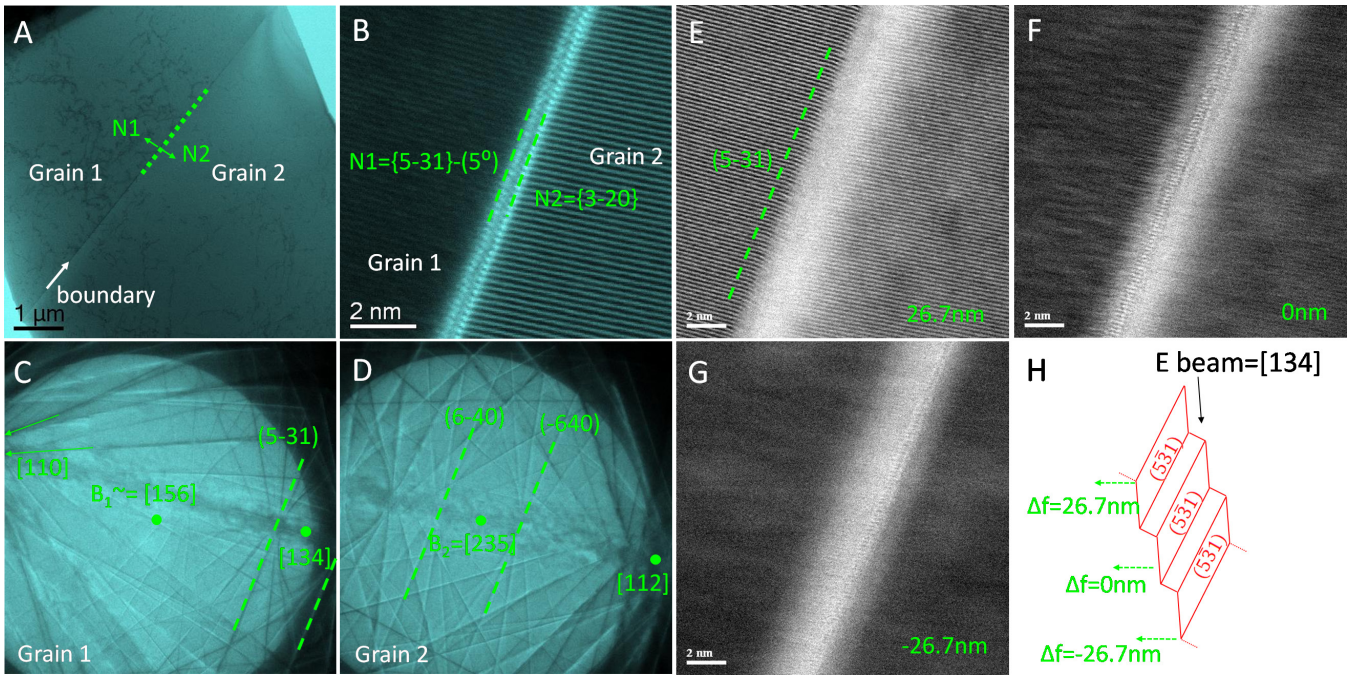


**Fig. S3**

Sample #1. (A) A low magnification bright field (BF) STEM image showing a planar boundary. The boundary was set to edge-on condition in (B). The Kikuchi patterns of the left grain and the right grain are given in (C) and (D), respectively. (E–G) Through-focal HAADF-STEM images of the boundary with the left grain was aligned to a [134] zone axis. Note that the {531} Kikuchi bands are parallel with the boundary plane. (H) A schematic diagram showing that the grain surface consisted of {531} terraces in the beam direction.

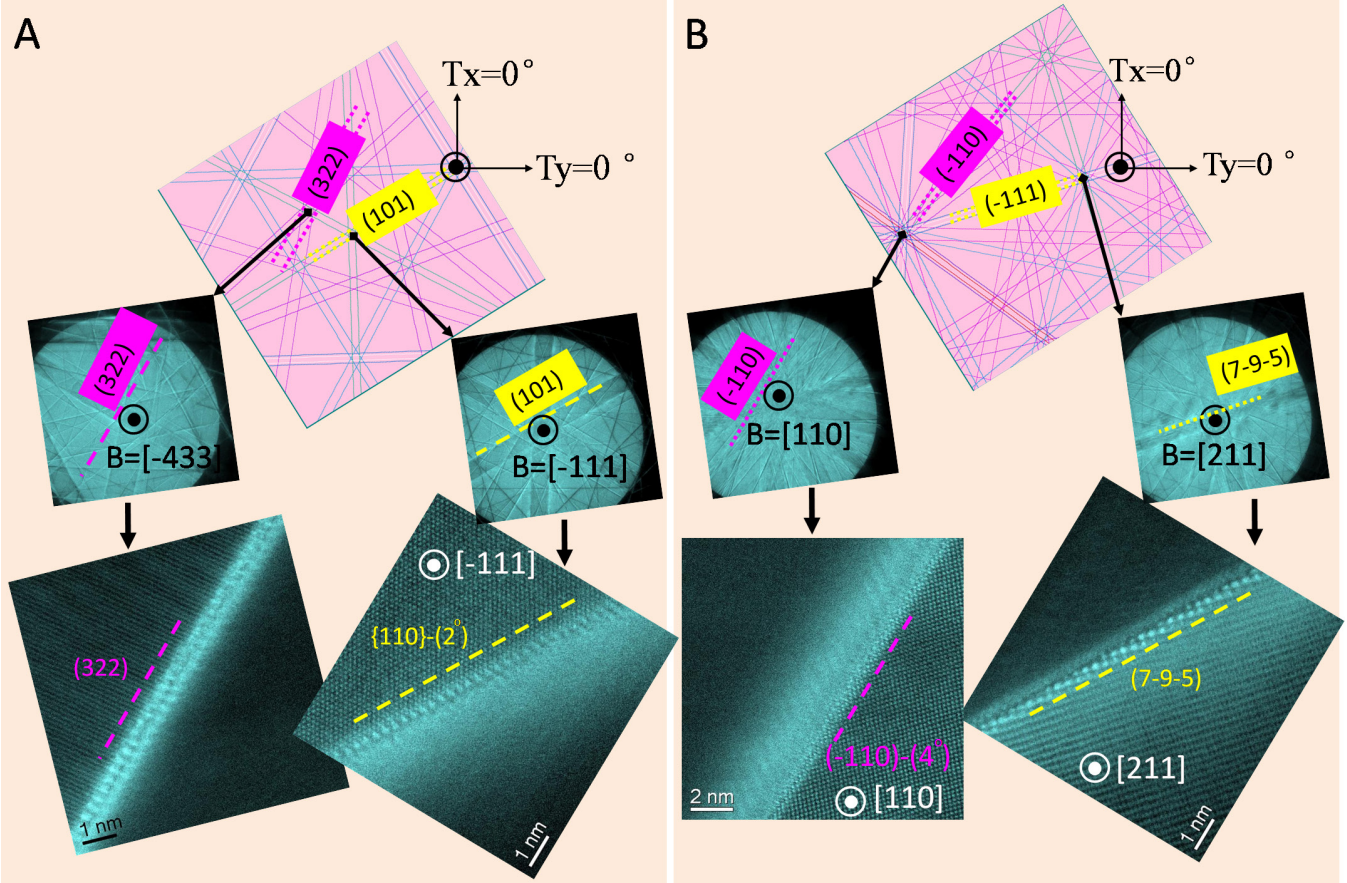


**Fig. S4**

Sample #2. (A) Identification of the boundary planes of the N1/N3 pairs. Inset (upper-left) was a low magnification HAADF-STEM image showing the alternate boundary faceting. The assignment of N1–N4 boundary planes is denoted in the inset. An enlarged Kikuchi map was attached for a better understanding of the crystallography. (B) Identification of the boundary planes of the N2/N4 pairs.

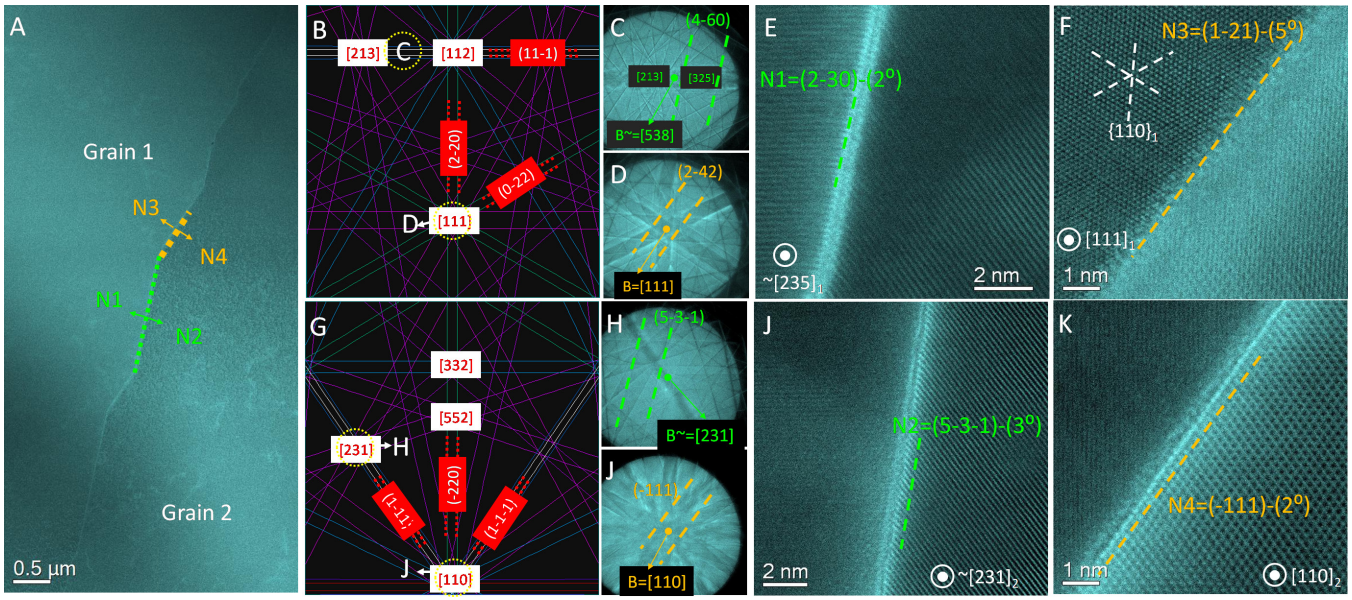


**Fig. S5**

Sample #3. (A) A low magnification HAADF-STEM image showing the alternate boundary faceting. The N1 and N3 boundary planes of the left grain were oriented to edge-condition in (E) and (F), respectively. The corresponding Kikuchi patterns were shown in (C) and (D), with an enlarged Kikuchi map shown in (B). Likewise, the N2 and N4 boundary planes of the right grain were identified in (G–K).

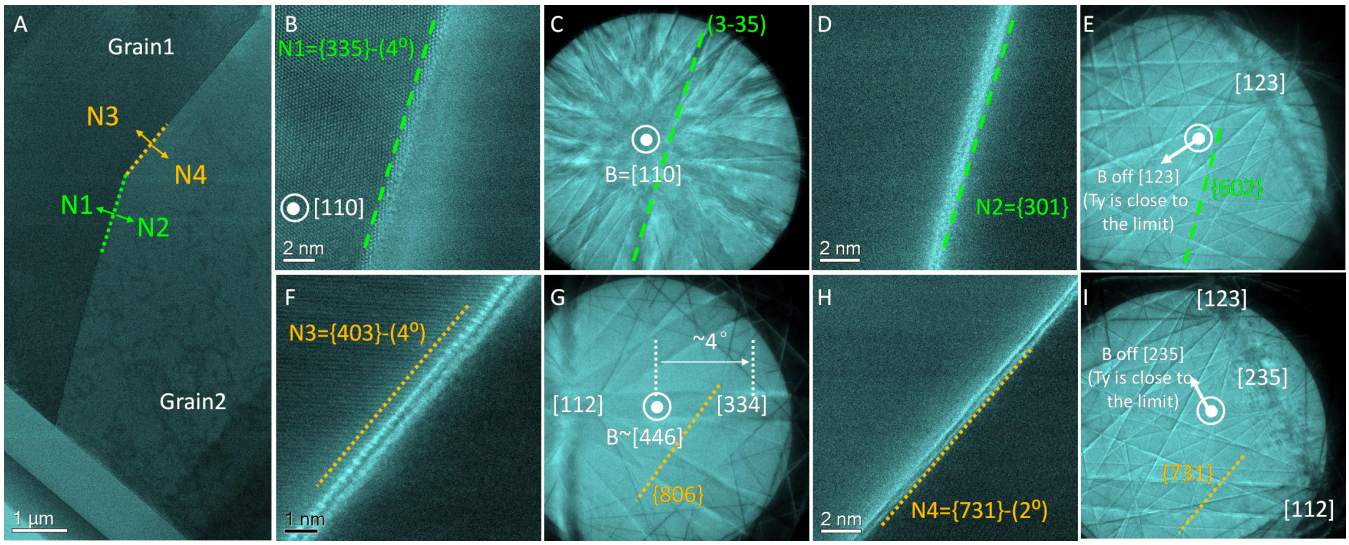


**Fig. S6**

Sample #4. (A) A low magnification HAADF-STEM image showing the alternate boundary faceting. The N1 and N3 boundary planes of the left grain were oriented to edge-condition in (B) and (F), respectively. The corresponding Kikuchi patterns were shown in (C) and (G). Likewise, the N2 and N4 boundary planes for the right grain were identified in (D, E) and (H, I).

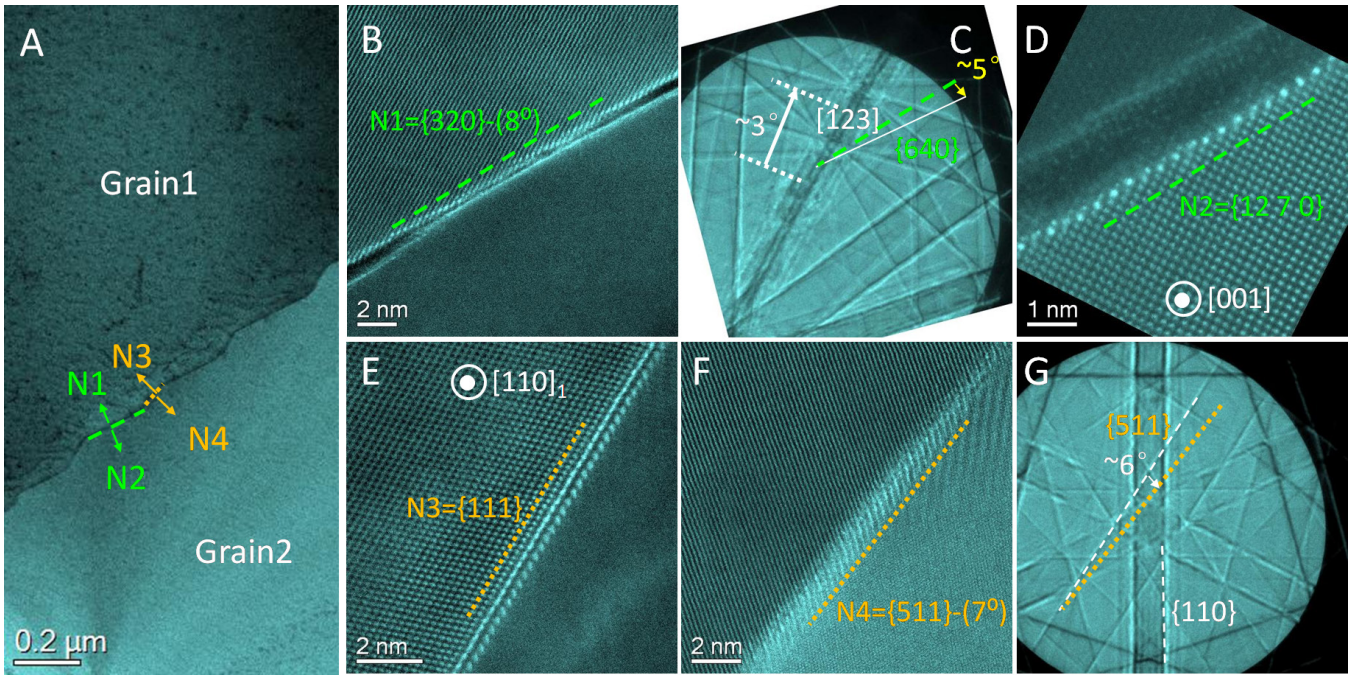


**Fig. S7**

Sample #5. (A) A low magnification HAADF-STEM image showing the alternate boundary faceting. The N1 and N4 grain surfaces were identified in (B, C) and (F, G) using Kikuchi patterns as a reference. The N2 (D) and N3 (E) boundary planes were determined via the two-dimensional lattice imaging method.

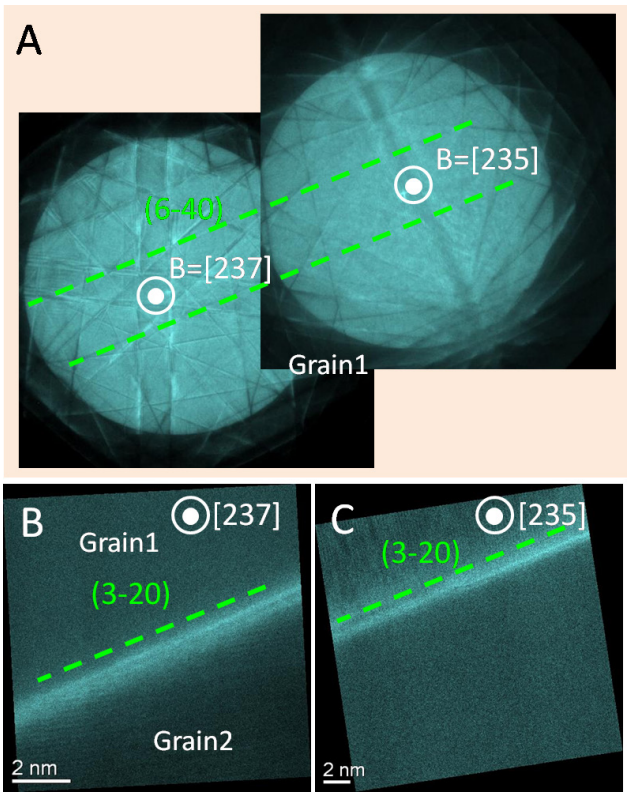


**Fig. S8**

Sample #6. Pairs of HAADF-STEM images and Kikuchi patterns used to identify a boundary plane. (A) Grain 1 was aligned to a [237] axis (left pattern) and a [235] axis (right pattern). (B) HAADF-STEM image of the edge-on boundary when the left grain was set to a [237] axis. (C) HAADF-STEM image of the edge-on boundary when the left grain was set to a [235] axis. Therefore, the normal of the boundary plane could be derived as a {320} plane (the cross product of [237] and [235] is the $(3\bar{2}0)$).

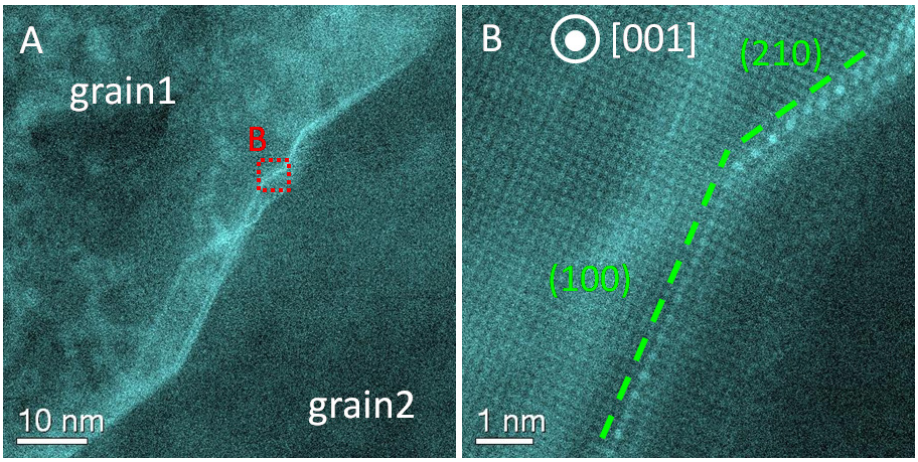


**Fig. S9**

Sample #7. (A) Low magnification HAADF-STEM image of a boundary with alternate faceting. (B) The boundary planes of the left grain were determined as (100) and (210) planes by high resolution HAADF-STEM imaging. Note the obvious Bi superstructures on the (210) plane and the (100) plane.

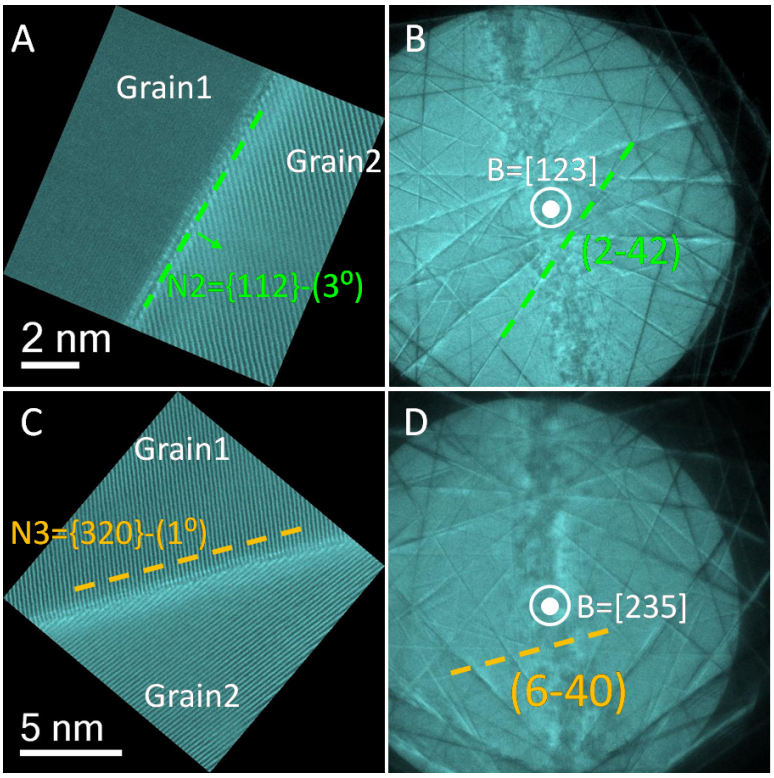


**Fig. S10**

Sample #8. Pairs of HAADF-STEM images and Kikuchi patterns that were used to identify the N2 (A, B) and the N3(C, D) boundary planes.

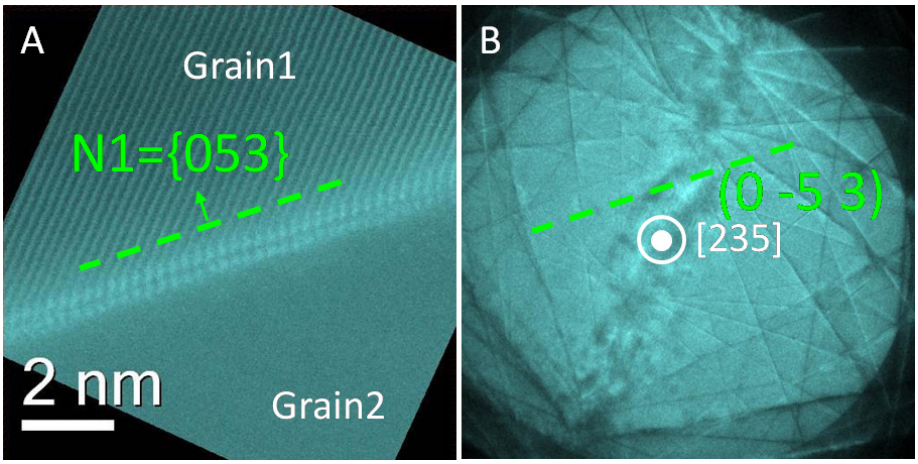


**Fig. S11**

Sample #9. (A, B) A HAADF-STEM image and its corresponding Kikuchi pattern that are used to identify the N1 boundary plane.

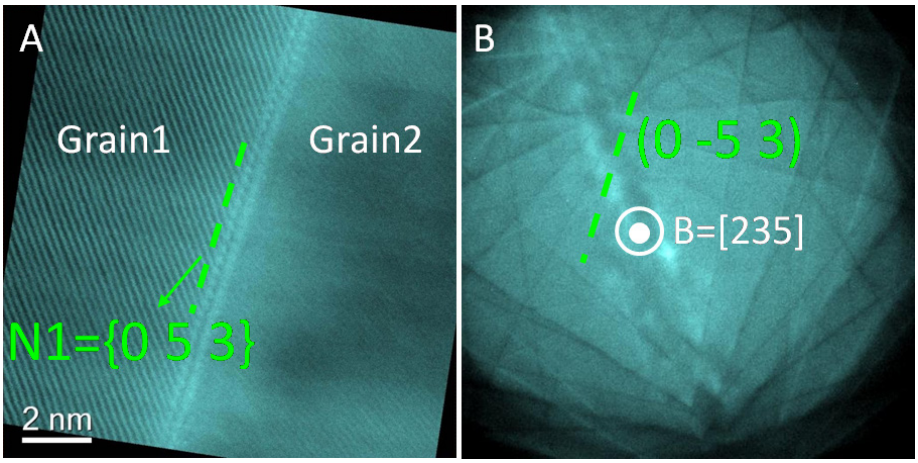


**Fig. S12**

Sample #10. (A, B) A HAADF-STEM image and its corresponding Kikuchi pattern that are used to identify the normal of the N1 boundary plane.

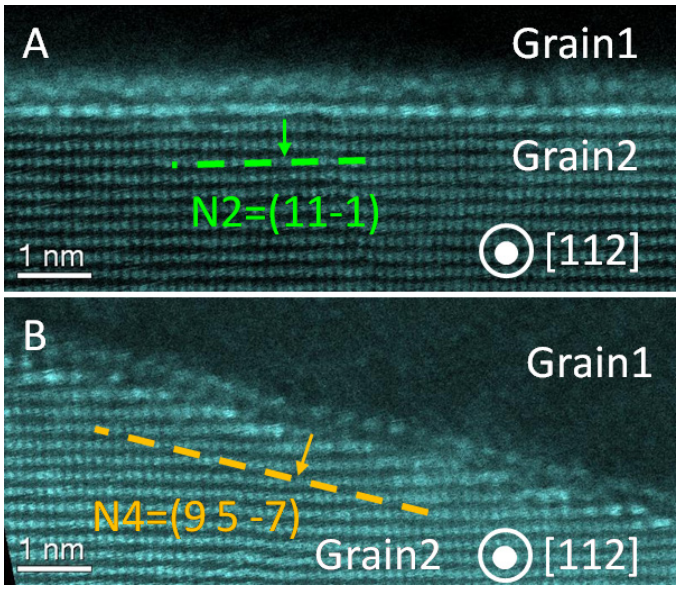


**Fig. S13**

Sample #11. Two high resolution HAADF-STEM images that are used to identify the normal of the N2 and N4 boundary planes of the lower grain ((A) N2, (B) N4).

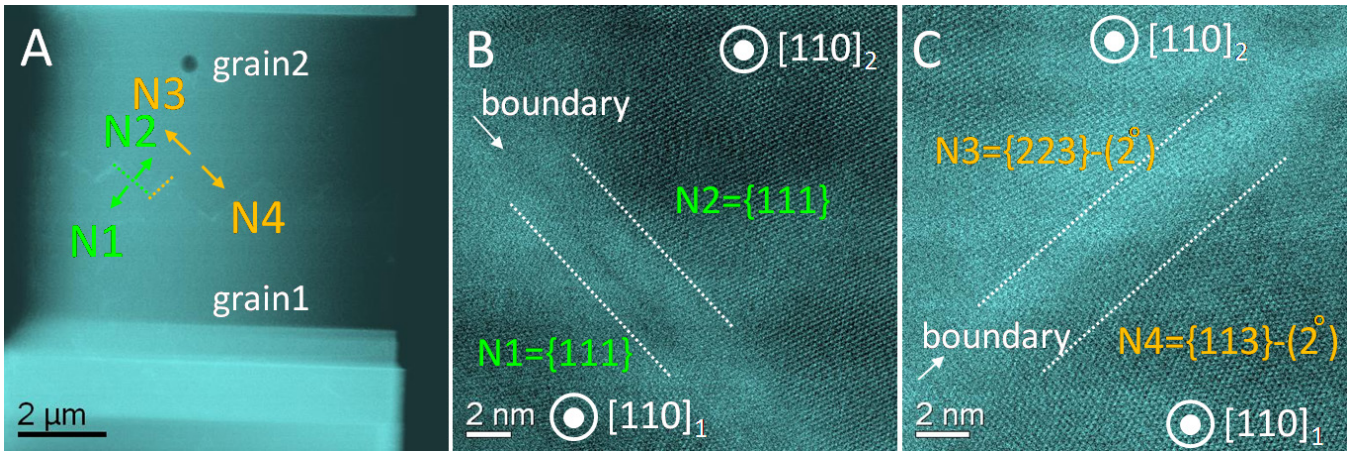


**Fig. S14**

Sample #12. (A) Low magnification HAADF-STEM image of a twin boundary. High resolution HAADF-STEM images of the two alternate facets were shown in (B) and (C) ((B) N1 and N2; (C) N3 and N4). No clear bilayer segregation and no Bi superstructures were observed on the {111}, {223} and {113} boundary planes. There might be a minor amount of Bi segregation at the boundaries if we considered the faint contrast variation at the interfaces (A), but EDS mapping of the boundaries suggested that the amount of Bi segregation was below the detection limit.

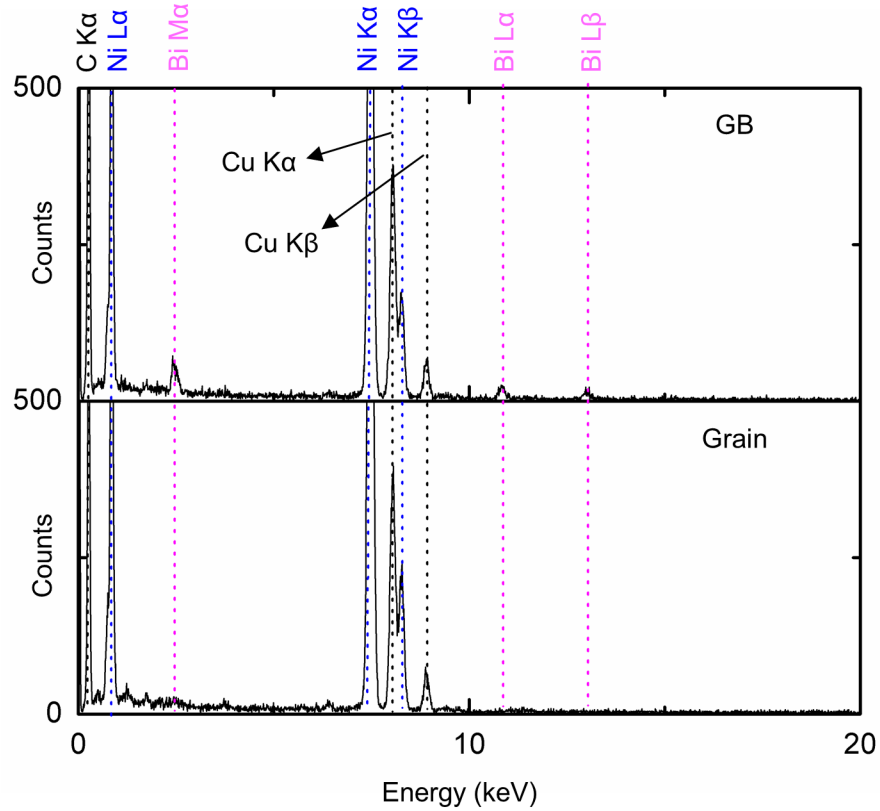


**Fig. S15**

Representative STEM-EDS spectra from a general Ni-Bi grain boundary ("GB") and grain interior ("Grain"). These spectra show that Bi M and L peaks were detected at the grain boundary but are absent from the grain, confirming that the grain boundary segregated atoms are Bi. Note that the C peak is present due to carbon contamination during probe scanning while the Cu signal arose from the Cu TEM grid.

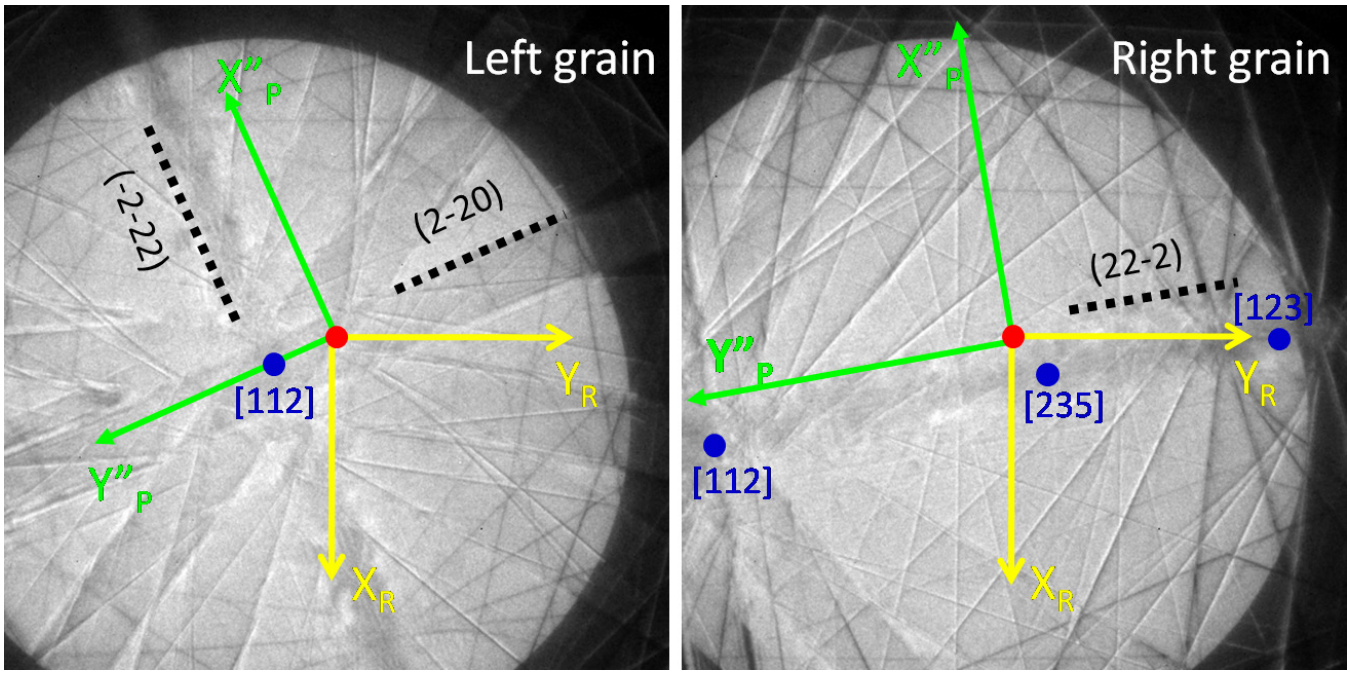


**Fig. S16**

An example showing the determination of the misorientation parameters in sample #2. Kikuchi patterns of the left grain and the right grain were recorded at the same sample tilt angle. The centers of screen were marked out by the red dots. The selection of the reference frame *RF* is indicated by ($X_R$, $Y_R$, $Z_R$) and the pattern frame PF by ($X_P$, $Y_P$, $Z_P$).

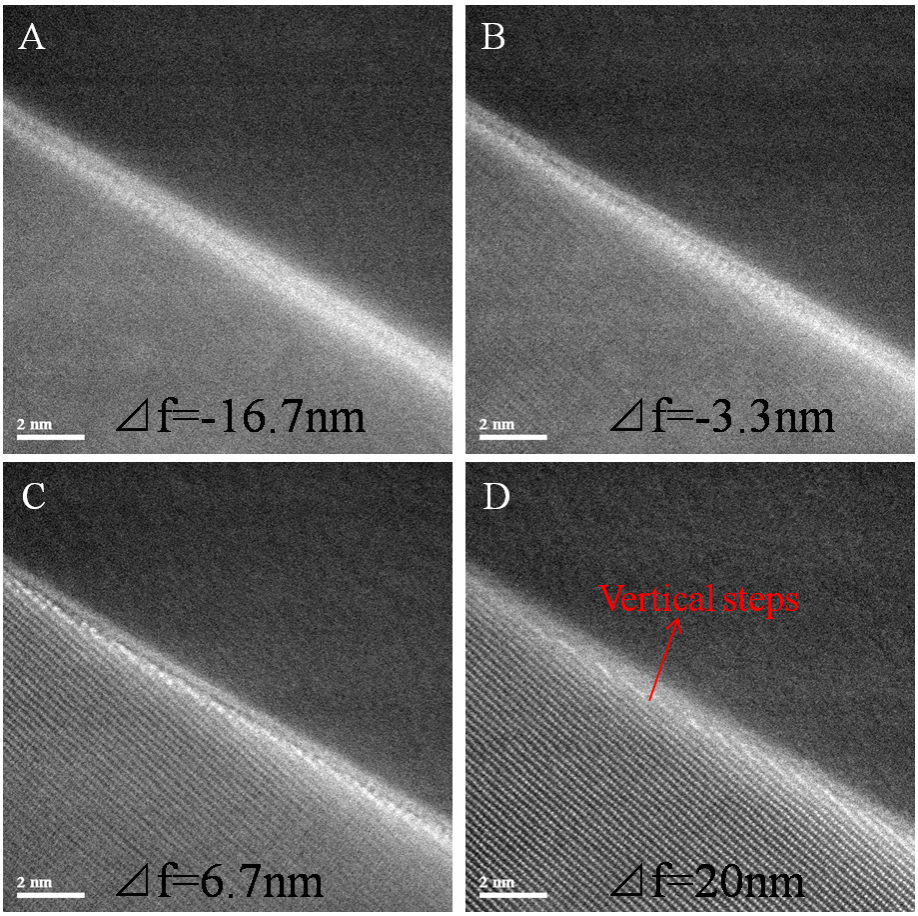


**Fig. S17**

Through-focal HAADF images of the N4 facet in Fig. 3E. There are some vertical steps along the beam direction, as marked out by red arrows in (D). It should be noted that, the projected grain boundary width is narrow. Those vertical steps are minor and could only be discerned in panel (D).

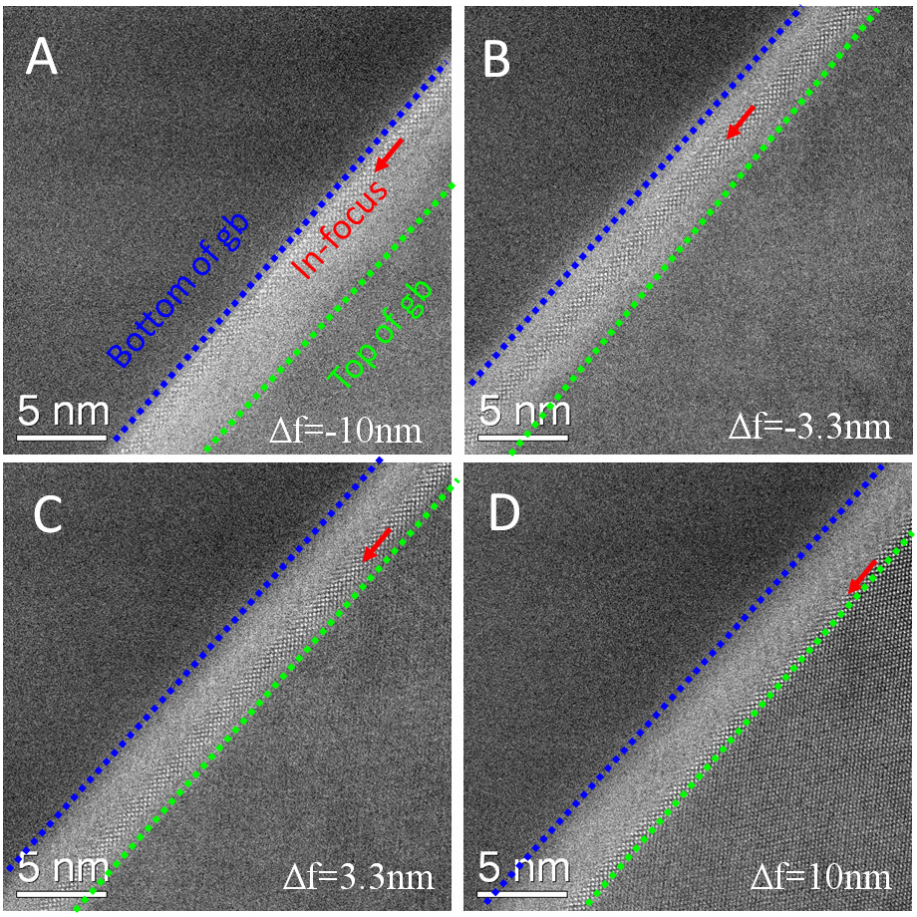


**Fig. S18**

Through-focal HAADF-STEM images of the N2 facet in Fig. 3C. When the focal planes were placed from the bottom of the grain boundary (blue dotted line) to the top of the grain boundary (green dotted line) step by step, the resolved layers were marked out by the red arrows. There are many steps in the beam direction. The steps are nearly periodic with some local roughness.

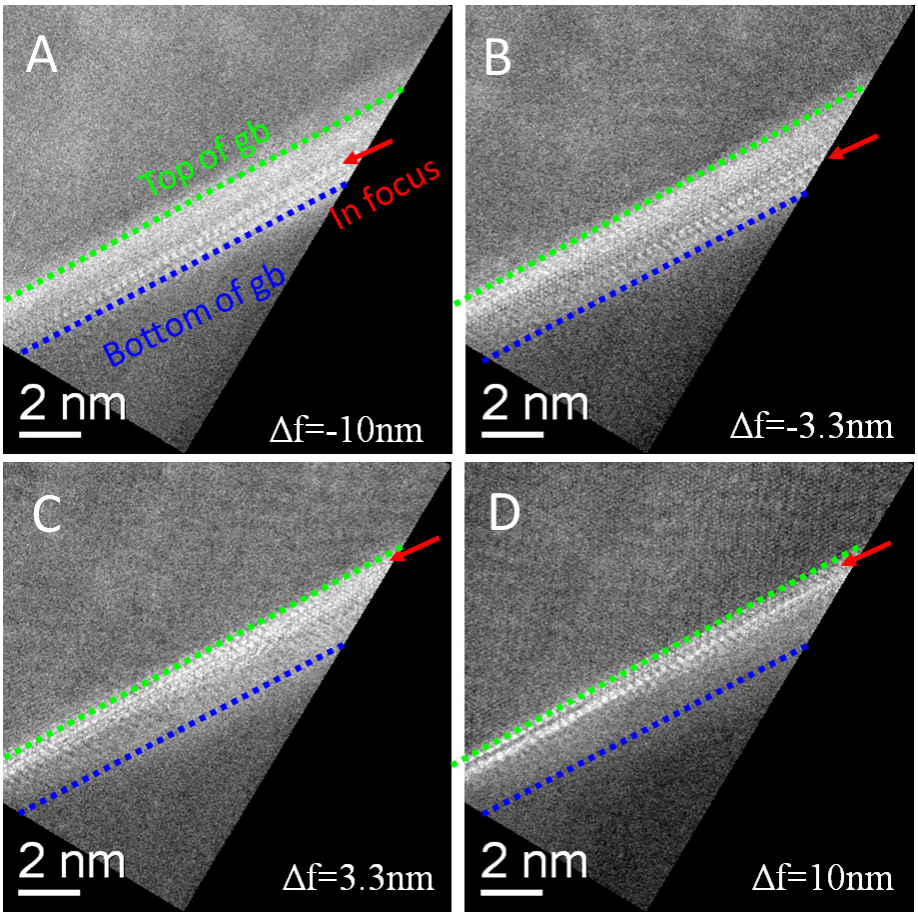


**Fig. S19**

Through-focal HAADF-STEM images of the N3 facet in Fig. 3D. The steps are nearly periodic with some roughness.

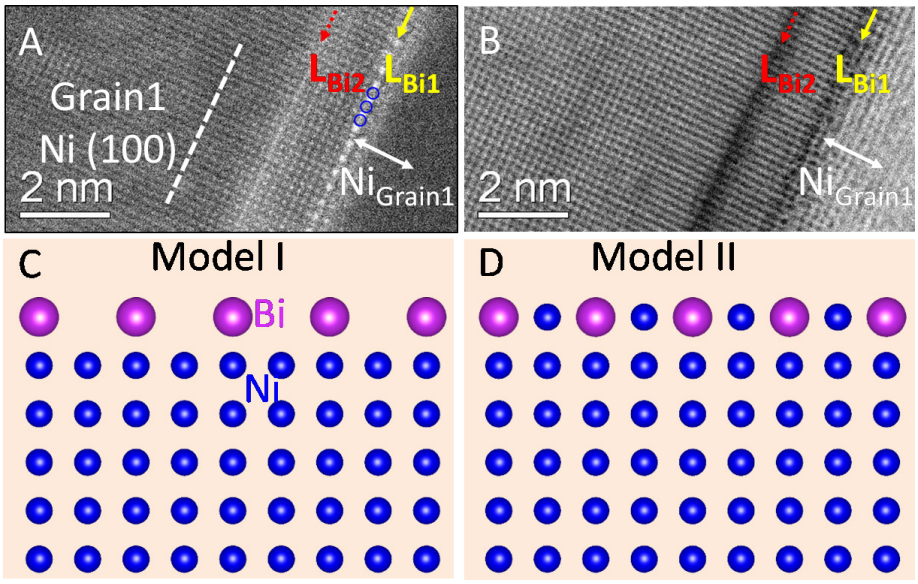


**Fig. S20**

(A, B) A pair of HAADF-STEM and BF-STEM images of a (100) grain boundary plane (Fig. 1C–D). The yellow arrow indicates an evident Bi layer (layer 1) while the red arrow denotes a second Bi layer (layer 2) with a relatively low contrast. The white arrows indicate the nickel lattice extending 2nm from layer 1. The blue circles in (A) indicate the presence of extra HAADF intensity in the middle of every two bright Bi columns. (C, D) Two possible atomic models of the Bi-rich structures on (100) grain surface. The model I is a C(2x2) Bi and an apparent 1Bi/2Ni superstructure while the model II consists of intermixed Bi and Ni atoms (surface alloying model).

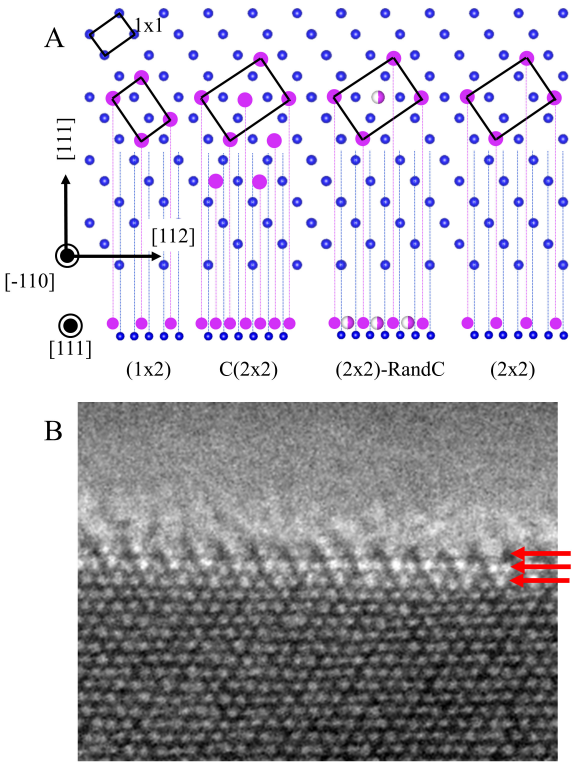


**Fig. S21**

(A) Four Bi superstructures on a $(1\bar{1}0)$ plane considered in surface DFT calculations. The upper diagram shows the plan views of the structures. The lower diagrams show the projected models along the [111] zone axis. Blue solid spheres are Ni atoms and purples ones are Bi atoms. In the (2x2)-RandC structure, the half-filled purple spheres represent Bi atoms that are randomly centered, such that they occur in every other cell of a C(2x2) structure. (B) In 2D projection, the raw HAADF-STEM image of a $(1\bar{1}0)$ boundary plane shows an apparent 3Bi/6Bi superstructure when viewed from this angle. Furthermore, there appears to be three layers of Bi atoms as indicated by the red arrows, but this apparent layering is just an artifact of atomic-scale steps in the [111] direction (i.e., into the page).

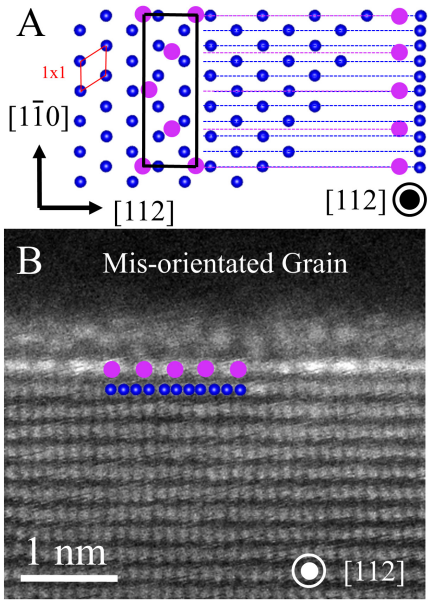


**Fig. S22**

(A) Left panel: Top view of the $[5\bar{5}11]$ Bi superstructure on a (111) surface. Right panel: the Bi superstructure is projected along the [112] direction that is aligned with the view direction in (B). (B) The raw HAADF-STEM image of a (111) grain surface showing an apparent 5Bi/10Ni superstructure in this projection.

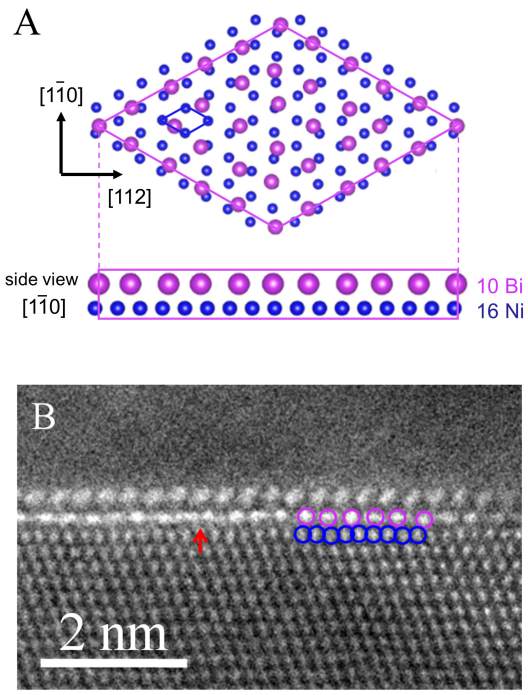


**Fig. S23**

(A) Upper panel: Top view of an (8x8) Bi superstructure on (111) surface. Lower panel: The Bi superstructure is projected along the [1$\bar{1}$0] direction, which is the same view direction as the HAADF-STEM image in (B). (B) The raw HAADF-STEM image of a (111) grain surface (Fig. 2K–L) showing how Bi atoms (pink circles) are arranged on Ni atoms (blue spheres) when viewed as a two-dimensional projection along the [1$\bar{1}$0] direction. Bi atoms have 10Bi/16Ni structure when viewed in this direction. The red arrow indicates the presence of local Bi disordering.

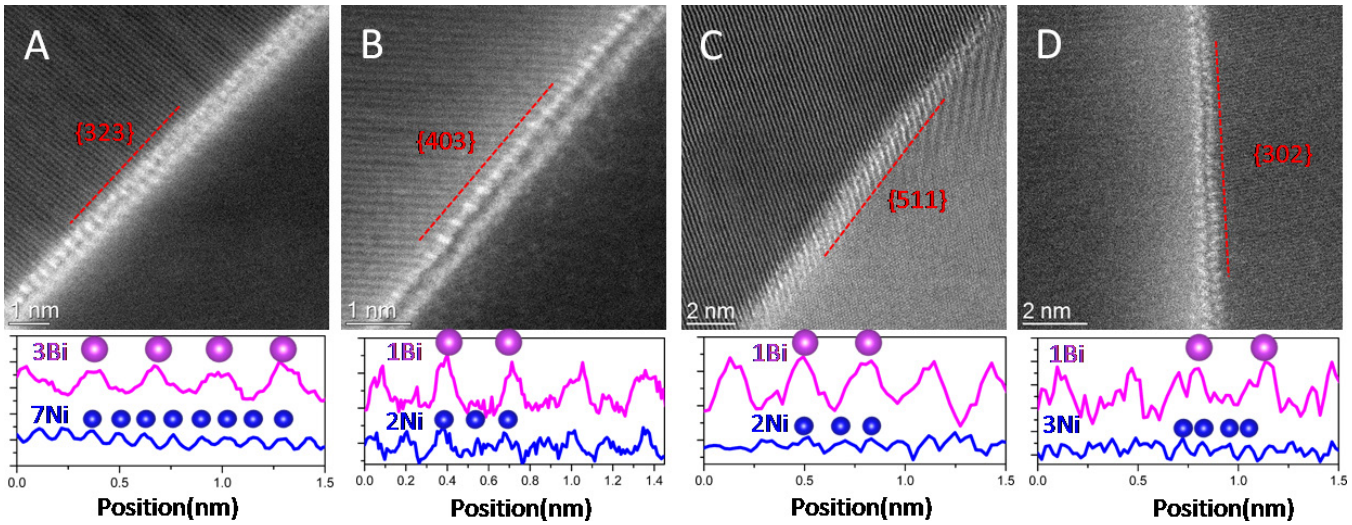


**Fig. S24**

Upper panels: HAADF-STEM images showing Bi superstructures on several boundary planes. Note that those images were recorded along high Miller index zone axes. Lower panels: Line profiles were taken along Bi columns (pink lines) and Ni lattices in the proximity of the interfaces (blue lines).

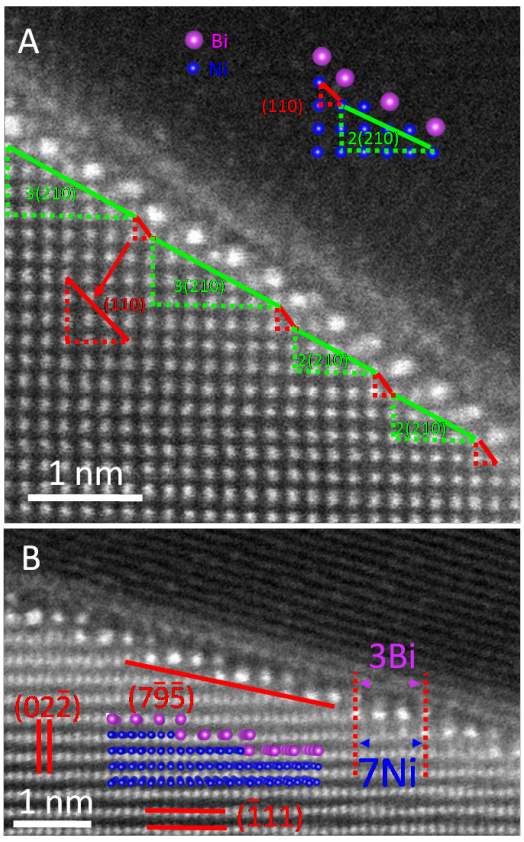


**Fig. S25**

High resolution HAADF-STEM images of Bi superstructures on two high index Ni grain surfaces. (A) An averaged (12 7 0) grain surface dissociates into a (7 4 0) segment and a (5 3 0) segment; each of these two nano-sized segments has two repeated units that can be considered as "1 (1 1 0) + 3 (2 1 0)" and "1 (1 1 0) + 2 (2 1 0)" atomic steps. The inset on the upper-right corner is a possible surface atomic structure that is supported by the DFT calculation. (B) An averaged {7 9 5} grain surface is composed of periodic (1 1 1) terraces and single atomic height steps parallel to $(02\bar{2})$; the repeat terraces are 7 Ni atoms wide, which can be interpreted as a 3Bi/7Ni superstructure.

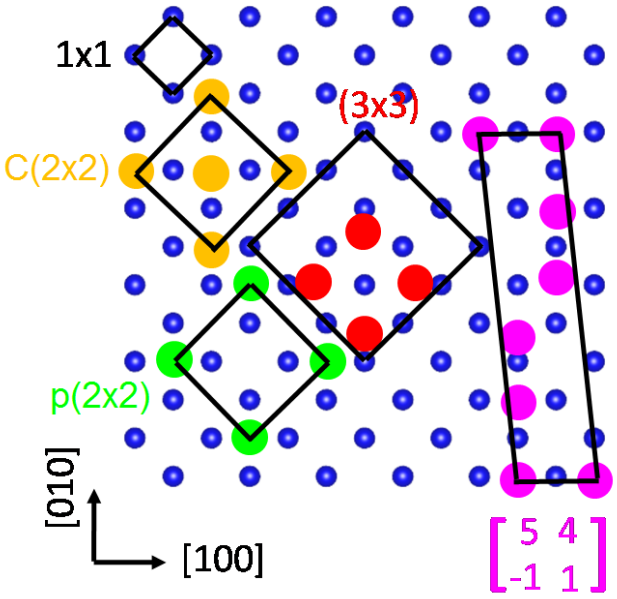


**Fig. S26**

Top view of the relaxed Bi monolayer structures on Ni(100). The calculated surface free energies of those structures are shown in Fig. 2A. Each Bi superstructure has the same color code in the structural models as it does in the line plot of the surface free energies.

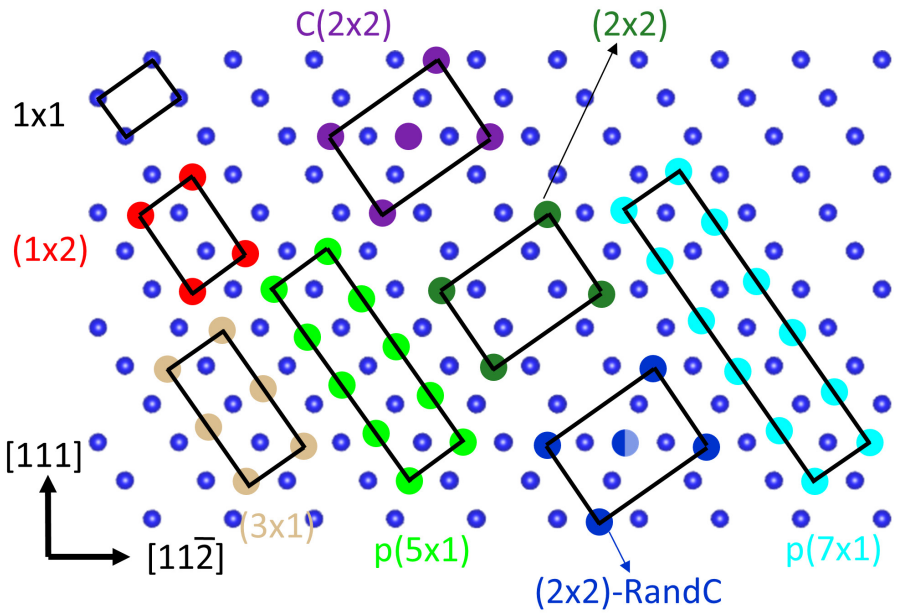


**Fig. S27**

Top view of typical relaxed Bi monolayer structures on Ni(110). The calculated surface free energies of those structures are shown in Fig. 2B. Each Bi superstructure has the same color code in the structural models as it does in the line plot of the surface free energies. The half-filled blue sphere in the (2x2)-RandC structure indicates that the Bi atoms are randomly centered, such that they appear in every other unit cell.

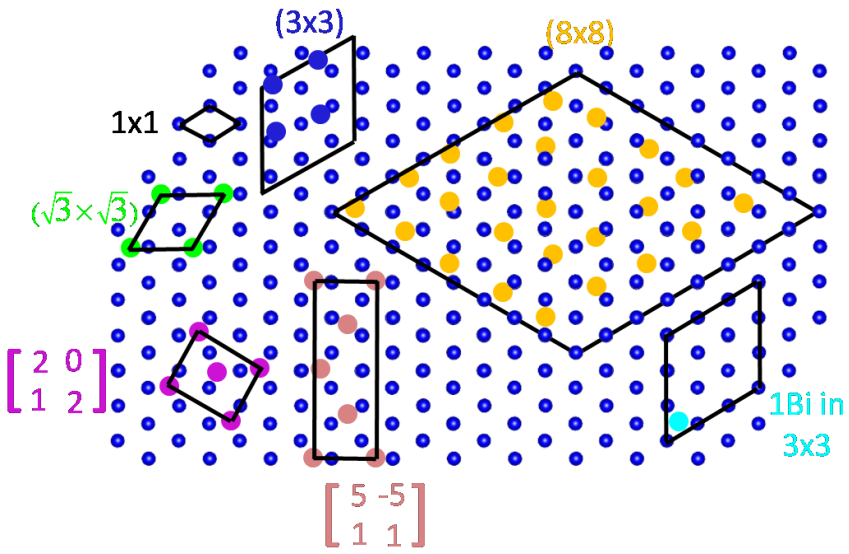


**Fig. S28**

Top view of typical relaxed Bi monolayer structures on Ni(111). The calculated surface free energies of those structures are shown in Fig. 2C. For convenience, we write the two matrices as [2012] and [5-511] in the text. Each Bi superstructure has the same color code in the structural models as it does in the line plot of the surface free energies.

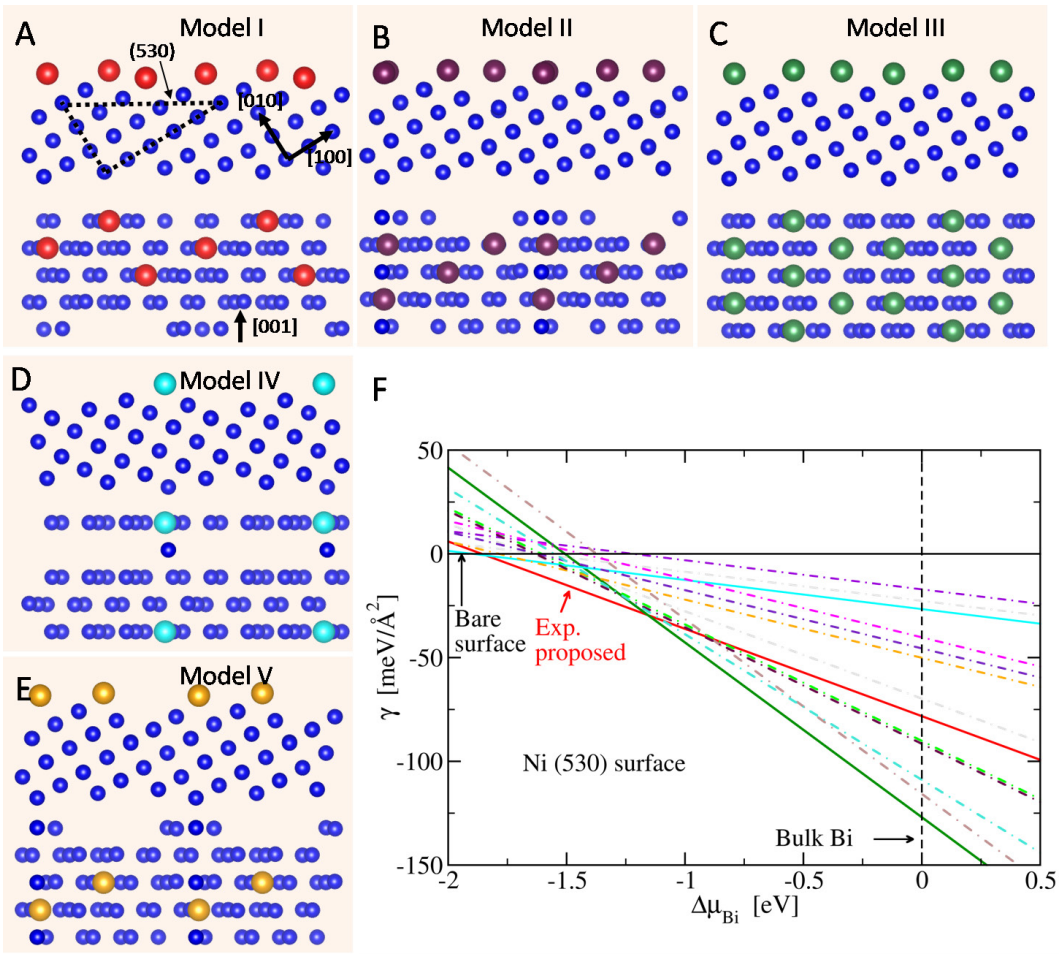


**Fig. S29**

(A–E) Upper panels: Side view of the relaxed Bi monolayer structures on Ni(530). Five different models are given (Models I–V). Model I matches the HAADF-STEM observation. Lower panels: Top view of the relaxed structures considered by surface DFT calculations. (F) The surface free energies of those structures. Each Bi superstructure has the same color code in the structural models as it does in the line plot of the surface free energies.

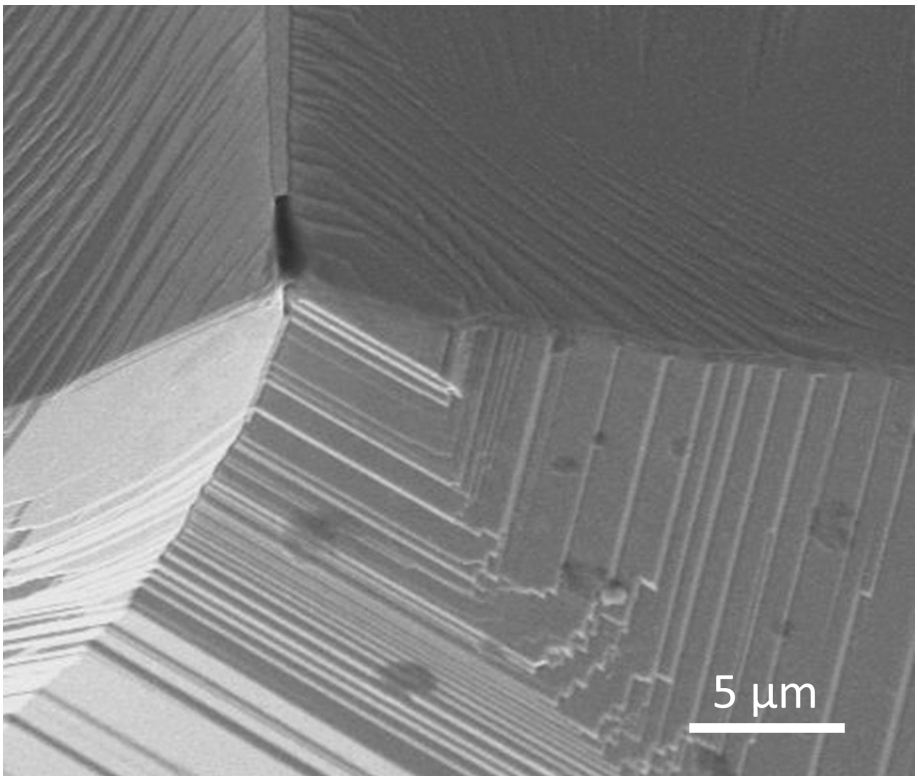


**Fig. S30**
SEM micrograph of an intergranular fracture surface in polycrystalline Bi-doped Ni. Micro-faceting is evident at all four general grain boundaries.

**Table S1.**

Summary of the grain boundary planes of twelve FIB-prepared TEM grain boundary samples. The errors from the actual planes to the identified planes are given in the brackets after the plane indices. The symbol "R" stands for reconstruction, indicating that Bi superstructures were observed. The coincident site lattice (CSL) Σ value was calculated using the misorientation data (*35*).

| Sample | Facet 1 | | Facet 2 | | Misorientation matrix (axis/angle notation) | CSL Σ value |
|---|---|---|---|---|---|---|
| **#1** | N1 | N2 | N3 | N4 | [0.9986 0.0473 0.0251<br>-0.0521 0.9668 0.2502<br>-0.0124 -0.2511 0.9679]<br>(14.8°/[ 0.979 0.194 0.073]) | $\Sigma > 500$ |
| | {531}-(5°) | {320} | - | - | | |
| **#2** | N1 | N2 | N3 | N4 | [-0.0473 -0.7452 -0.6652<br>0.9865 -0.1392 0.0858<br>-0.1565 -0.6521 0.7418]<br>(42.6°/[ 0.974 0.179 0.138]) | $\Sigma > 500$ |
| | {322}-R | {110}-(4°) | {110}-(2°)-R | {795}-R | | |
| **#3** | N1 | N2 | N3 | N4 | 0.0056 -0.2666 0.9638<br>0.8221 0.5499 0.1473<br>-0.5693 0.7915 0.2222]<br>(37.9°/ [ 0.910 0.398 0.115]) | $\Sigma > 500$ |
| | {320}-(2°) | {531}-(3°) | {112}-(5°) | {111}-(2°) | | |
| **#4** | N1 | N2 | N3 | N4 | [0.8038 -0.5944 -0.0254<br>0.5614 0.7436 0.3632<br>-0.1970 -0.3063 0.9313]<br>(42.3°/ [0.858 0.497 0.127]) | $\Sigma > 500$ |
| | {335}-(4°) | {301} | {430}-(4°)-R | {731}-(2°) | | |
| **#5** | N1 | N2 | N3 | N4 | [-0.1595 -0.0882 -0.9833<br>-0.9286 -0.3246 0.1797<br>-0.3350 0.9417 -0.0302];<br>(22.1°/ [0.878 0.452 0.158]) | $\Sigma > 500$ |
| | {320}-(8°) | {12 7 0}-R | {111}-R | {511}-(7°)-R | | |
| **#6** | {320} | | | | [0.7654 -0.5203 0.3788<br>0.6020 0.7869 -0.1354<br>-0.2276 0.3316 0.9155];<br>(42.8°/ [1.000 1.298 2.403]) | $\Sigma > 500$ |
| **#7** | {100}-R&{210}-R | | | | [0.7101 -0.3073 0.6335<br>0.6997 0.4082 -0.5863<br>-0.0784 0.8596 0.5049];<br>(53.4°/ [-1.669 -2.6642 -1.000]) | $\Sigma > 500$ |
| **#8** | {112}-(3°)&{320}-(1°) | | | | [-0.0680 -0.9971 -0.0333<br>0.9711 -0.0585 -0.2314<br>0.2288 -0.0481 0.9723]<br>(14.0°/ [-1.000 -5.654 1.554]) | $\Sigma > 500$ |
| **#9** | {530} | | | | [0.9840 0.1777 0.0109<br>-0.1776 0.9755 0.1299<br>0.0124 -0.1298 0.9915];<br>(12.7°/ [-170.64 -1.00 -233.43]) | $\Sigma > 500$ |
| **#10** | {530} | | | | [0.3459 0.3497 0.8706<br>-0.7835 -0.4029 0.4731<br>0.5162 -0.8458 0.1347];<br>(41.4°/ [1.000 -1.6908 -1.8974]) | $\Sigma > 500$ |
| **#11** | {111}-R&{795}-R | | | | [ 0.8604 0.0618 -0.5058<br>-0.2303 0.9327 -0.2777<br>0.4546 0.3554 0.8167];<br>(36.4°/ [2.167 -3.288 -1.000]) | $\Sigma > 500$ |
| **#12** | {111}&{223}-(2°)&{113}-(2°) | | | | 70.8°/ [1 1 0] | $\Sigma = 3$ twin |

**Table S2.**

The dissociation of boundary planes into low Miller index structural units. We present them using a terrace-step notation. The numbers before the indices of the terraces denote the width of terraces. For instance, the {795} consists of {111} terraces, seven atoms wide, separated by {110} steps with single-atom-height.

| Boundary plane indices | Terrace | Step |
|---|---|---|
| **{115}** | 2{001} | {111} |
| **{214}** | 4{111} | {210} |
| **{317}** | 3{102} | {011} |
| **{315}** | 4{111} | {110} |
| **{112}** | 2{111} | {100} |
| **{335}** | 3{111} | {001} |
| **{223}** | 4{111} | {100} |
| **{795}** | 7{111} | {110} |
| **{301}** | {201} | {100} |
| **{503}** | 2{201} | {101} |
| **{302}** | {201} | {101} |
| **{403}** | 2{201} | {001} |